DYNAMIC STALL CHARACTERISTICS OF
DROOPED LEADING EDGE AIRFOILS

Final Report

Submitted to

NASA Ames Research Center
Attn: Dr. Chee Tung
Aeromechanics Branch
Army/NASA Rotorcraft Division
Mail Stop T12-B
Moffett Field, CA 94035-1000

Prepared by

Lakshmi N. Sankar
Regents' Professor

Mehmet Sahin and Naveen Gopal
Graduate Research Assistants
School of Aerospace Engineering
Georgia Institute of Technology
Atlanta, GA 30332-0150

Phone: 404-894-3014
E-Mail: lsankar@ae.gatech.edu

BACKGROUND

Helicopters in high-speed forward flight usually experience large regions of dynamic stall over the retreating side of the rotor disk. The rapid variations in the lift and pitching moments associated with the stall process can result in vibratory loads, and can cause fatigue and failure of pitch links. In some instances, the large time lag between the aerodynamic forces and the blade motion can trigger stall flutter.

A number of techniques for the alleviation of dynamic stall have been proposed and studied by researchers. Passive and active control techniques have both been explored. Passive techniques include the use of high solidity rotors that reduce the lift coefficients of individual blades, leading edge slots and leading edge slats. Active control techniques include steady and unsteady blowing, and dynamically deformable leading edge (DDLE) airfoils. Considerable amount of experimental and numerical data has been collected on the effectiveness of these concepts.

One concept that has not received as much attention is the drooped-leading edge airfoil idea. It has been observed in wind tunnel studies and flight tests that drooped leading edge airfoils can have a milder dynamic stall, with a significantly milder load hysteresis. Drooped leading edge airfoils may not, however, be suitable at other conditions, e.g. in hover, or in transonic flow. Work needs to be done on the analysis and design of drooped leading edge airfoils for efficient operation in a variety of flight regimes (hover, dynamic stall, and transonic flow). One concept that is worthy of investigation is the dynamically drooping airfoil, where the leading edge shape is changed roughly once-per-rev to mitigate the dynamic stall.

SUMMARY OF WORK

1. An existing 2-D dynamic stall solver developed by the principal investigator and his graduate students (Jiunn-Chi Wu, Ph. D. Dissertation, 1987) was modified. The modifications included incorporation of a new one-equation turbulence model, and a transition model. The modified code was validated for a NACA 015 airfoil undergoing sinusoidal oscillations, for which experimental data by Pizhiali are

available. Appendix A summarizes the code validation studies, documented as a Master's special problem (mini-thesis) by Mr. Mehmet Sahin.

2. In parallel to the study of drooped leading edge airfoils, work was done on a dynamic leading edge concept in collaboration with Dr. Chee Tung of NASA Ames Research Center, and Dr. Chandrasekhara of the Naval Postgraduate School. This work had been initiated before the present grant was in place, and continued during the grant. Appendix B includes a recent AIAA publication summarizing the findings.

3. Calculations were done for a drooped leading edge airfoil. This airfoil is derived from a base-line VR 12 airfoil, with the leading edge region rotated down to produce a drooped-leading edge. This particular configuration has been studied in a water tunnel by McAlister et al. Numerical simulations have also been attempted by Wang et al using an incompressible Navier-Stokes solver. Three set of flow conditions (mild stall or attached flow, moderate stall, deep stall) were considered in this investigation for the two airfoils- VR-12 and modified VR-12. Appendix C describes the calculations in detail. The following conclusions can be drawn.

   a) At low angles of attack ($\alpha = 11°\pm4°$), both airfoils experienced attached flow. The maximum lift $C_{l,max}$, the maximum drag $C_{d,max}$, as well as the maximum nose-down pitching moments were comparable for the two airfoils.

   b) At moderate angles of attack, ($\alpha = 14°\pm4°$), the baseline airfoil experienced a mild stall, with the attendant rise in drag and nose-down pitching moment. The drooped leading airfoil did not stall at all. An examination of the flow field indicated that this desirable behavior is a consequence of the milder adverse pressure gradient in the nose region of the drooped leading edge airfoil. The conventional airfoil has a high suction peak, and a rather steep adverse pressure gradient and is more prone to stall.

   c) At higher angles of attack, ($\alpha = 21°\pm4°$), both airfoils experienced dynamic stall. Even under such a severe condition, dropped airfoil had more desirable characteristics (smaller hysteresis, lower $C_{d,max}$, lower maximum nose-down pitching moments).

CONCLUDING REMARKS

A 2-D dynamic stall solver has been improved with the addition of a nw turbulence model and a transition model. Several validation studies have done, prior to the application of this solver to two promising dynamic stall alleviation concepts: a drooped elading edge airfoil, and a dynamically deformed elading edge airfoil. Both concepts showed promising improvements in the dynamic stall characteristics compared to the baseline airfoil. Additional studies over a wider range of Mach numbers and reduced frequencies is needed to further evaluate these two concepts.

APPENDIX A

Code Validation Studies

VALIDATION OF 2-D UNSTEADY NAVIER-STOKES SOLVER CODE (DSS2) FOR SEVERAL DYNAMIC STALL TEST CASES

Mehmet SAHIN

20 July 2000

Advisor: L. SANKAR

INTRODUCTION

The stalling of helicopter rotor blades occurs on the retreating side of the rotor disc. When stall occurs, the blade dynamics and elastic properties become important in determining the subsequent changes in angle of attack and aerodynamic loads. The dynamic stall loads can reduce the fatigue life of helicopter rotors by unacceptable amounts and requires replacement of critical part of rotors. This can be avoided by defining flight boundaries which restrict the aircraft operation in regions away from dynamic stall. However helicopters are being considered for tasks force vehicle designers to consider dynamic stall region which make dramatic increase in performance envelope of aircraft.

The features of dynamic stall regimes are characterized by the degree of viscous-inviscid interaction taking place in the flow field. When the viscous layers rapidly thicken and becomes larger, it is a strong viscous-inviscid interaction. McCroskey and Pucci [1] collected dynamic stall regimes into four groups depending on degree of viscous-inviscid interaction. They are

No stall – Weak interactions

Stall onset – Mild interactions

Light stall – Strong interactions

Deep stall – Viscous Dominant

Among four most challenging and difficult ones are the light and deep stall regimes. Light stall shows general features of static stall, but unsteady separation and extend of strong viscous inviscid interactions are the primary features of this regime. Boundary layer thickness can be order of airfoil thickness during the stall. Deep stall, on the other hand, characterized by highly non-linear pressure fluctuations and large region of vortical structure over the lifting surface. During the deep stall boundary layer thickness can be order of airfoil chord length. The deep dynamic stall phenomenon involves three phases. The lift initially increases as the airfoil pitches up, and continues to increase well past the static stall value, $C_{l,max}$. Towards the end of the upstroke, a vortex begins to form near the leading edge and grows in strength. Towards the beginning of the down-stroke, or shortly thereafter, this vortex is shed from the upper surface, creating a rapid loss in the bound circulation and lift. As this vortex rolls downstream over the upper surface, it causes large reductions in local pressure, and high nose down pitching moments. As the airfoil pitches down, one or more weaker vortices are shed from the upper surface, creating additional fluctuations in lift and pitching moment. The flow eventually reattaches at lower angles of attack.

5

In the recent years Reynolds number, reduced frequency, compressibility, transition, turbulence and three dimensional effects on dynamic and static stalls have been studied. The dynamic stall at low Reynolds numbers is generally a trailing edge stall. As the Reynolds number increase the type of airfoil stall during dynamic motion changed from trailing to leading edge stall [2,3]. The decreased in reduced frequency generally increases intensity of dynamic stall shedding. The lower reduced frequency causes early formation of leading edge vortex. Compressibility effects studied at [4-6] and cause increase in vorticity strength within the boundary layer. Because velocity at the outer edge of the boundary layer is higher compare to incompressible flow. Additionally increase in density at the downstream of the flow cause to strengthen the vorticity due to angular momentum conservation. This phoneme typically occur just after the minimum suction point over the airfoil. This increase in vorticity strength causes early formation of leading edge vortex. Transition and turbulence modeling are still challenging subject in fluid dynamic and studied at [7-9].

In this study Baldwin-Lomax and Spalart-Allmaras turbulence models was used to show turbulence modeling effects on dynamic stall. In addition to turbulence models Eppler's and Mitchel's transition criterions was used to predict transition point over the pitching airfoil. A computational work was done for the validation of two-dimensional unsteady Navier-Stokes code for several dynamic stall test cases. Previous validation studies are given in [8].

In here two different test cases were chosen. The first one corresponds to no-stall case around the NACA0015 airfoil at a Reynolds number of 1955000, a Mach number of 0.2895 and a reduced frequency of 0.095. The angle of attack was changed -0.2^0 to 8.2^0 with mean angle of attack 4.0^0. The second one was light dynamic stall case of the NACA0015 airfoil at similar free stream conditions with a reduced frequency of 0.095. The angle of attack was changed between 6.66^0 to 15.10^0 with mean angle of attack 10.88^0.

The completed first two cases showed that turbulence modeling has significant effect on dynamic stall at higher angle of attacks. For the first case there is no significant difference between these two turbulence models. However Baldwin-Lomax method found to be insufficient for the light stall case. On the other hand Spalart-Allmaras turbulence model gives better result for the same case. Transition is believed to have important effect on dynamic stall during the down-stroke motion and at lower angle of attacks with a mild pressure gradient. However predicted transition points are very close to leading edge and flow seems to be fully turbulent.

GOVERNING EQUATIONS

It has been show by Viviand [10] that it is possible to write the transformed governing unsteady Reynolds averaged Navier-Stokes equations in strong conservative form as

6

$$\frac{\partial(Q)}{\partial\tau} + \frac{\partial(E_I - E_V)}{\partial\xi} + \frac{\partial(F_I - F_V)}{\partial\eta} = 0$$

Q the vector of conserved variables

$$Q = \frac{1}{J}\begin{bmatrix} \rho \\ \rho u \\ \rho v \\ e \end{bmatrix}$$

E_I and F_I the convective flux vectors

$$E_I = \frac{1}{J}\begin{bmatrix} \rho U \\ \rho Uu + \xi_x p \\ \rho Uv + \xi_y p \\ (e+p)U - \xi_t p \end{bmatrix} \qquad F_I = \frac{1}{J}\begin{bmatrix} \rho V \\ \rho Vu + \eta_x p \\ \rho Vv + \eta_y p \\ (e+p)V - \eta_t p \end{bmatrix}$$

E_V and F_V the flux vectors for viscous terms

$$E_V = \frac{1}{J}\begin{bmatrix} 0 \\ \xi_x \tau_{xx} + \xi_y \tau_{xy} \\ \xi_x \tau_{xy} + \xi_y \tau_{yy} \\ \xi_x(u\tau_{xx} + v\tau_{xy} - q_x) \\ + \xi_y(u\tau_{xy} + v\tau_{yy} - q_y) \end{bmatrix} \qquad F_V = \frac{1}{J}\begin{bmatrix} 0 \\ \eta_x \tau_{xx} + \eta_y \tau_{xy} \\ \eta_x \tau_{xy} + \eta_y \tau_{yy} \\ \eta_x(u\tau_{xx} + v\tau_{xy} - q_x) \\ + \eta_y(u\tau_{xy} + v\tau_{yy} - q_y) \end{bmatrix}$$

Where $J = \xi_x \eta_y - \xi_y \eta_x$ and defined to be metric Jacobian.

The metric terms are calculated from

$$\frac{\xi_t}{J} = y_\tau x_\eta - x_\tau y_\eta \qquad \frac{\eta_t}{J} = x_\tau y_\xi - y_\tau x_\xi$$

$$\frac{\xi_x}{J} = y_\eta \qquad \frac{\xi_y}{J} = -x_\eta$$

$$\frac{\eta_x}{J} = -y_\xi \qquad \frac{\eta_y}{J} = x_\xi$$

The contravariant velocity components U and V are defined as

$$U = \xi_t + \xi_x u + \xi_y v \qquad V = \eta_t + \eta_x u + \eta_y v$$

The total energy per unit volume is

$$e = \frac{p}{\gamma - 1} + \frac{\rho}{2}\left(u^2 + v^2\right)$$

And stagnation enthalpy per unit mass is

7

$$h_o = \frac{\gamma p}{\rho(\gamma - 1)} + \frac{1}{2}\left(u^2 + v^2\right)$$

The viscous stress tensor is

$$\tau_{ij} = \mu\left[\frac{\partial u_j}{\partial x_i} + \frac{\partial u_i}{\partial x_j} - \frac{2}{3}\left[\frac{\partial u_i}{\partial x_i}\right]\delta_{ij}\right] - \rho\overline{u_i'u_j'}$$

The Reynolds-stresses $-\rho\overline{u_i'u_j'}$ are modeled according to the Boussinesq approximation which allows one to take Reynold-stresses into account simply by modifying the viscosity. Thus viscous stresses can be written as

$$\tau_{ij} = (\mu + \mu_T)\left[\frac{\partial u_j}{\partial x_i} + \frac{\partial u_i}{\partial x_j} - \frac{2}{3}\left[\frac{\partial u_i}{\partial x_i}\right]\delta_{ij}\right] - \rho\overline{u_i'u_j'}$$

where μ_T is a turbulent viscosity coefficient. The heat fluxes calculated from

$$q_i = -\frac{c_p}{Pr}(\mu + \mu_T)\frac{\partial T}{\partial x_i}$$

where Pr is the Prandtl number

The equations are non-dimensionalized as follows

$$x^* = x/L \qquad t^* = t/(L/c_\infty) \qquad e^* = e/\rho_\infty c_\infty^2$$
$$y^* = y/L \qquad \rho^* = \rho/L \qquad \mu^* = \mu/\mu_\infty$$
$$u^* = u/c_\infty \qquad T^* = T/T_\infty \qquad \mu_T^* = \mu_T/\mu_\infty$$
$$v^* = v/c_\infty \qquad p^* = p/\rho_\infty c_\infty^2$$

Here L is the reference length, c_∞ is the free stream speed of sound, ρ_∞ is the free-stream density, T_∞ is the free stream temperature and μ_∞ is the free stream viscosity. In the following the asterisks are omitted for simplicity. The present scaling retains the form of the inviscid fluxes, whereas the stress terms have to be multiplied by M_∞/Re_∞ and the non-dimensionalized heat flux terms have to be multiplied by $M_\infty/(\gamma - 1)Pr_\infty Re_\infty$.

SPALART-ALLMARAS TURBULENCE MODEL

The value of eddy viscosity is obtained from modified eddy viscosity $\tilde{v}$, which obeys the following non-dimensional partial differential equation [11].

$$\frac{D\tilde{v}}{Dt} = c_{b1}\tilde{S}\tilde{v} + \frac{M_\infty}{Re_\infty}\frac{1}{\sigma}\left[\nabla \cdot \left((v + \tilde{v})\nabla\tilde{v}\right) + c_{b2}(\nabla\tilde{v})^2\right] - \frac{M_\infty}{Re_\infty}\left[c_{w1}f_w\right]\left[\frac{\tilde{v}}{d}\right]^2$$

8

where the first term at right hand side represents production. The second term are called first and second order diffusion terms. The third term is destruction of $\tilde{v}$. In here the eddy viscosity v_T is given by

$$v_T = \tilde{v} f_{v1}$$

where

$$f_{v1} = \frac{\chi^3}{\chi^3 + c_{v1}^3} \quad \text{and} \quad \chi = \frac{\tilde{v}}{v}$$

Here S is the vorticity strength and

$$\tilde{S} \equiv S + \frac{M_\infty}{Re_\infty} \frac{\tilde{v}}{\kappa^2 d^2} f_{v2}$$

Also d is the distance to the closest wall and

$$f_{v2} = 1 - \frac{\chi}{1 + \chi f_{v1}}$$

The function f_w is given by the following expression

$$f_w = g \left[\frac{1 + c_{w3}^6}{g^6 + c_{w3}^6} \right]^{1/6}$$

Where

$$g = r + c_{w2}\left(r^6 - r\right)$$

$$r = \frac{M_\infty}{Re_\infty} \frac{\tilde{v}}{\tilde{S}\kappa^2 d^2}$$

TRANSITION MODELING

The above equation is applicable to fully turbulent flow without laminar boundary layers and transitions. In many aerodynamic problems there are typically both laminar and turbulent boundary layers and position of the transition point can not be predicted accurately. In Spalart-Almaras turbulence model transition effects are modeled by modifying the production and destruction terms. The modified equation is given by

9

$$\frac{D\tilde{v}}{Dt} = c_{b1}\left[1 - f_{t2}\right]\tilde{S}\tilde{v} + \frac{M_\infty}{Re_\infty}\frac{1}{\sigma}\left[\nabla \cdot \left((v + \tilde{v})\nabla\tilde{v}\right) + c_{b2}(\nabla\tilde{v})^2\right] - \frac{M_\infty}{Re_\infty}\left[c_{w1}f_w - \frac{c_{b1}}{\kappa^2}f_{t2}\right]\left[\frac{\tilde{v}}{d}\right]^2$$

These modifications ensure a laminar solution at the upstream of the flow. f_{t2} parameter is calculated from:

$$f_{t2} = c_{t3}\exp\left(-c_{t4}\chi^2\right)$$

To initiate the transiton near the trip points an additional term is added

$$\frac{D\tilde{v}}{Dt} = c_{b1}\left[1 - f_{t2}\right]\tilde{S}\tilde{v} + \frac{M_\infty}{Re_\infty}\frac{1}{\sigma}\left[\nabla \cdot \left((v + \tilde{v})\nabla\tilde{v}\right) + c_{b2}(\nabla\tilde{v})^2\right] - \frac{M_\infty}{Re_\infty}\left[c_{w1}f_w - \frac{c_{b1}}{\kappa^2}f_{t2}\right]\left[\frac{\tilde{v}}{d}\right]^2 + \frac{M_\infty}{Re_\infty}f_{t1}\Delta U^2$$

The trip function f_{t1} is computed as follows. Let d_t be the distance from the field point to the nearest trip point, which is on a wall. Let the quantity S_t be the wall vorticity at the trip location, and ΔU the norm of the difference between the velocity at the trip and at the field point we are considering. Then one can compute an intermediate quantity $g_t = \min(0.1, \Delta U/S_t\Delta x)$ where Δx is the grid spacing along the wall at the trip point. Then f_1 Parameter can be calculated as follows:

$$f_{t1} = c_{t1}g_t\exp\left(-c_{t2}\frac{S_t^2}{\Delta U^2}\left[d^2 + g_t^2 d_t^2\right]\right)$$

The model coefficients are:

$c_{b1}=0.1355$, $\sigma = 2/3$, $c_{b2}= 0.622$, $\kappa = 0.41$,

$c_{w1} = c_{b1}/\kappa^2 + (1+c_{b2})/\sigma$, $c_{w2}=0.3$, $c_{w3}=2$, $c_{v1}=7.1$, $c_{t1}=1$, $c_{t2}=2$ $c_{t3}=1.1$, $c_{t4}=2$.

In addition Spalart-Allmaras transition model Eppler's [12] and Mitchel's [13] transition criterions are used to predict transition points over the pitching airfoil. The laminar boundary layer quantities such as the momentum thickness δ_2, energy thickness δ_3, and the shape factor $H_{32}=\delta_3/\delta_2$ are computed using Thwaites' method [14]. The velocity at the edge of the boundary layer u_e is calculated from pressure at the airfoil surface. According to Eppler transition criterion transition occurs at:

$$\log\left(\frac{u_e\delta_2}{v}\right) > 18.4H_{32} - 21.74 - 0.34r$$

Here r is a roughness factor and for highly polished surfaces it may be taken to be zero. According to Michel's Transition Criterion transition is occur at:

$$R_{\delta_2} = 1.174 \left(1 + \frac{22400}{R_x}\right) R_x^{0.46}$$

were R_x is the Reynolds number based on length from the stagnation point.

BOUNDARY CONDITIONS

Boundary conditions are applied on the airfoil surface and at outer boundaries. On the airfoil surface adiabatic, no-slip boundary conditions are imposed by setting contravariant velocity components to zero. Pressure and density are extrapolated from the interior and total energy is found by using the perfect gas relations. The value of eddy viscosity is set to zero on the airfoil surface. At the outer region one dimensional flow assumption is used to define the incoming and outgoing characteristics. Therefore, at inflow boundary, all the conservative variables are fixed to their free stream and at the outflow extrapolation is used for the conserved variables except pressure is fixed if the outflow is subsonic. The eddy viscosity is set to zero for inflow and extrapolated for the outflow boundary conditions.

NUMERICAL DISCRITIZATION

For discritation of Navier-Stokes equation a local time linearization is used [15].

$$E^{n+1} = E^n + \frac{\partial E^n}{\partial Q} \Delta Q^{n+1} = E^n + A^n \Delta Q^{n+1}$$

$$F^{n+1} = F^n + \frac{\partial F^n}{\partial Q} \Delta Q^{n+1} = F^n + B^n \Delta Q^{n+1}$$

Application of above equation produce delta form

$$\left[I + h\delta_\xi A^n + h\delta_\xi B^n\right] \Delta Q^{n+1} = -h\left[\delta_\xi E^n + \delta_n F^n\right]$$

Where A and B are Jacobian matrices. The resulting algebraic system can be solved directly by taking advantage of its sparse structure. However it will be very costly in both CPU time and memory. One way to simplify the solution is to introduce approximation factorization.

$$\left[I + h\delta_\xi A^n\right]\left[I + h\delta_\xi B^n\right] \Delta Q^{n+1} = -h\left[\delta_\xi E^n + \delta_n F^n\right]$$

11

Second order accurate central differences are used to discritize the above equation.To damp high frequency oscillations and maintain stability in supersonic region a numerical dissipation model described at Ref. [16] is used.

Similarly Spalart-Allmaras turbulence equation are discritized by using secon-order accurate central differences at the right hand side of the equation and first-order upwind differences is used on the implicit left hand side. The resulted algebraic equations are solved by using approximate factorization.

NUMERICAL EXPERIMENTS

The first validation case corresponds to no-stall case around the NACA0015 airfoil at a Reynolds number of 1955000, a Mach number of 0.2895 and a reduced frequence of 0.095 based on half chord. The airfoil pitching motion is described by: $\alpha = 4.0° + 4.2° \cos(\omega t)$. In this case Baldwin-Lomax turbulence model was used and flow assumed to be fully turbulent or fully turbulent just after the trip location. However there is no significant differences between two cases since the trip location very close to the leading edge.

To show the effect of grid intensity on numerical solution four different grid resolution was used. The grid resolution along the chord-wise and normal directions are respectively 257X65, 257X129, 513X65 and 513X129. Time step fixed to 0.005. The comparison of computed results with the experiment was shown in Fig.1. The presented results show very good agreement and nearly grid independent. However as the grid resolution increased the computed results deviate from the experimental value. Which is belived that only increase of grid resolution is not enough to increase accuracy without decreasing to time step in order to keep the CFL number constant. Time step effect on numerical solution was also studied on course grid and was presented in Fig.2. As expected the solution was getting better as the time step was reduced. Additionally in this case pressure coefficient distribution over the airfoil at several different angle of attack is compared with the experimental value and was presented in Fig.3. During the upstroke motion of the airfoil calculated results show very good agreement with experimental data however during downstroke close to zero angle attach there is a slight difference in pressure distribution. It is believed to be effect of transition point which moves downwards at small angle of attacks due to mild pressure gradient.

The second one was light dynamic stall of the NACA0015 airfoil at a Reynolds number of 1955000, Mach number of 0.2895 and a reduced ferquency of 0.095. The angle of attack changed with $\alpha = 10.88° + 4.22° \cos(\omega t)$. In this case only a coarse grid is used to solve the flow field. The calculated results on the coarse grid shown on Figure 4 show that there is a significant difference between Baldwin-

Lomax and Spalart-Allmaras turbulence models. It is seen that the Spalart-Allmaras model does a better job of capturing the hysteresis effects.

The effects of transition point location on light stall are shown in Fig.5. The transition point was allowed to move with the angle of attack. Eppler's transition criterion generally gives transition point closer to leading edge compare to Michel's transition criterion. However, when the flow separates over the airfoils Eppler's criterion gives wrong location and a jump in transition point.

CONCLUSIONS

The computed results show that Baldwin-Lomax turbulence model gives very good result for attached flow but it is not adequate to model light stall. Spalart-Allmaras model gives better results compare to Baldwin-Lomax model at higher angle of attacks.

Both transition models used here gives transition point on the upper surface close to the leading edge during the upstroke due to high pressure gradient and results are similar to fully turbulent case. During the dowstroke after light stall Michel's criterion gives a transition point close to leading edge but Eppler's criterion gives a transition point close to trailing edge.

REFERENCES

1. McCroskey W.J., Pucci L.S. "Viscous-Inviscid Interaction on Oscillating Airfoils in Subsonic Flow", AIAA Journal, Vol. 20, No. 2, 1982, pp.167-174.

2. Mehta U.B., "Dynamic Stall of Oscillating Airfoil", AGARD CP227, AGARD Meeting on Unsteady Aerodynamics, Paper No.23, Ottawa, September 1977.

3. Philippe J.J., "Dynamic Stall: An Example of Strong Interactions Between Viscous and Inviscid Flows', AGARD CP 227, AGARD Meeting on Unsteady Aerodynamics, Paper No.21, Ottawa, September 1977.

4. Sankar N.L. and Tassa Y., "Compressibility effects on Dynamic Stall of a NACA0012 Airfoil", AIAA Journal, Vol. 19, No. 5, pp. 557-568.

5. Visbal M.R., "Effect of Compresibility on Dynamic Stall of a Pitching Airfoil", AIAA Journal of Aircraft, Vol. 27, May 1990, pp. 400-407.

6. VanDyken R. and Chandrasekhara M. "Leading Edge Velocity Field of an Oscillating Airfoil in Compressible Dynamic Stall", AIAA-92-0193, 30th AIAA Aerospace Science Meeting, Reno, NV, January 6-9 1992.

7. Davidson L. and Rizzi A., "Navier-Stokes Computation of Airfoil in Stall Using Algebraic Reynold-Stress Model", AIAA Paper 92-0195, January 1992.

8. Wu, J.C., Huff D.L.and Sankar L.N., "Evaluation of Three Turbulence Models in Static Air Loads and Dynamic Stall Predictions", AIAA Journal of Aircraft, Vol. 27, No. 4, 1990, pp. 382-384.

9. Dindar M., Kaynak U. "Effect of Turbulence Modeling on Dynamic Stall of a NACA0012 Airfoil", AIAA Paper, 92-0027, January 1992.

10. Viviand H., "Conservative Forms of Gas Dynamic Equations", LeRecherche Aerospatiale, No:1, January-February 1974, pp.65-68.

11. Spalart P.R. and Allmaras S.R., "A One-Equation Turbulence Model for Aerodynamic Flows", AIAA Paper 92-0439, January 1992.

12. Eppler, R., Airfoil Design and Data, New York, NY, Springer-Verlag, 1990, 562 pp.

13. R. Michel, et al, "Stability Calculations and Transition Criteria on Two- or Three-Dimensional Flows," Laminar-Turbulent Transition, Novosibirsk, USSR, July 9-13, 1984, pp. 455-461.

14. Thwaites, B., "Approximate calculation of the laminar Boundary layer," Aeronautical Quarterly, Vol. 1, 1949, pp.245-280.

15. Pulliam T.H., "Implicit Finite-Difference Method for the Euler Equations", AIAA Paper 83-0344, January 1983.

16. Swanson R.C. and Turkel E., "Artificial Dissipation and Central Difference Schemes for the Euler and Navier-Stokes Equations", AIAA Paper 87-1107, January 1987.

Effect of grid resolution on Cl-Alpha versus
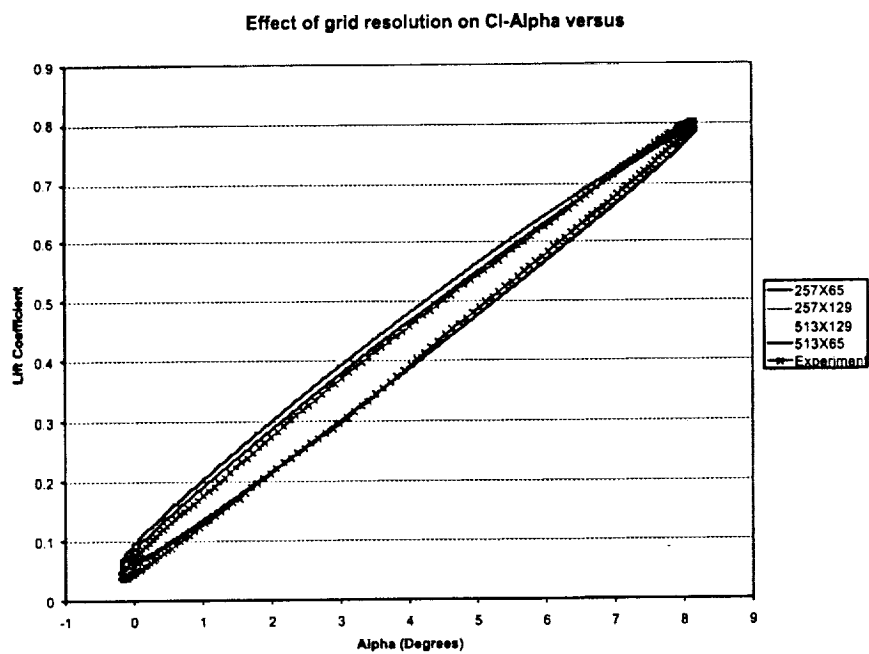
Figure 1 a. Effect of Grid Size on Lift Hysteresis Loop

Effect of grid resolution on Cd-Alpha versus
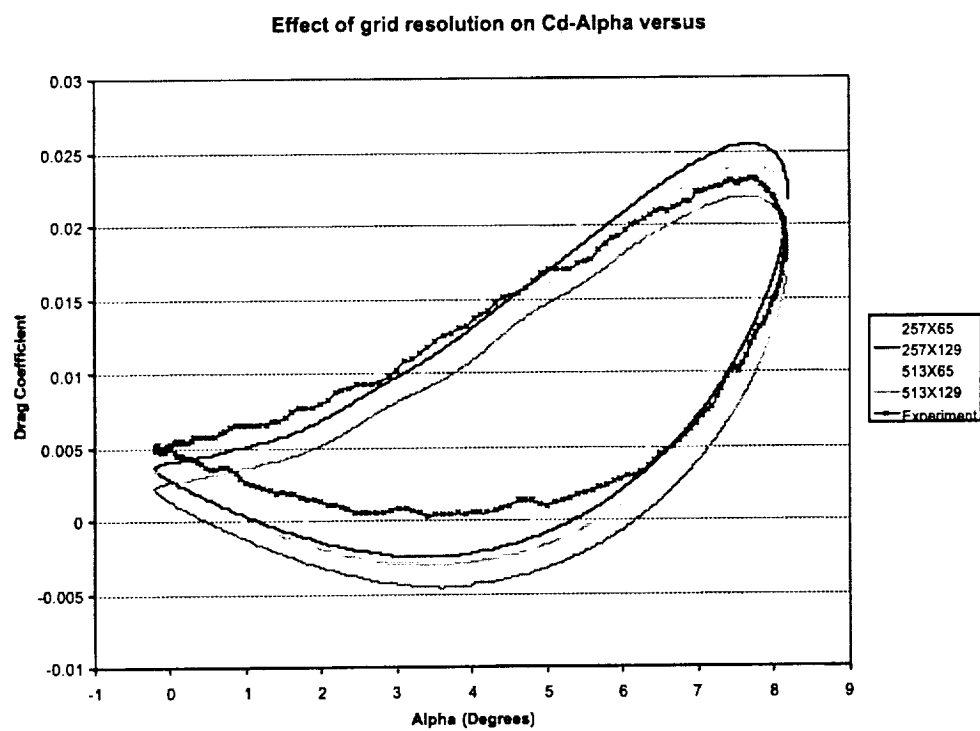
Figure 1 b. Effect of Grid Size on Drag Hysteresis Loop

Effect of grid resolution on Cm-Alpha versus
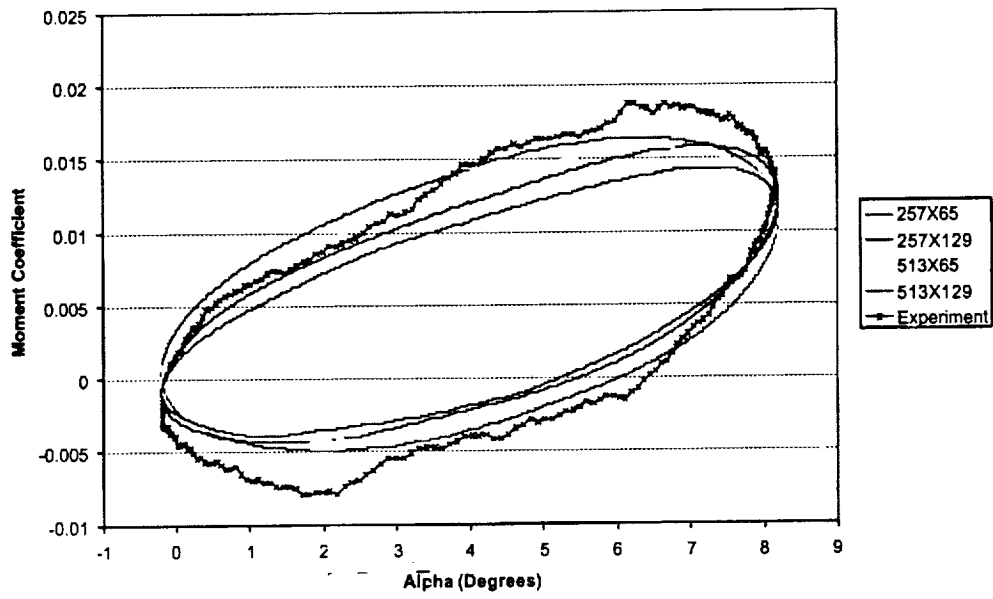
Figure 1 c. Effect of Grid Size on Pitching Moment Hysteresis Loop

Effect of time step on Cl-Alpha versus on 257X65 grid

| — delt=0.0025 | — delt=0.0050 | — delt=0.0100 | —•— Experiment |
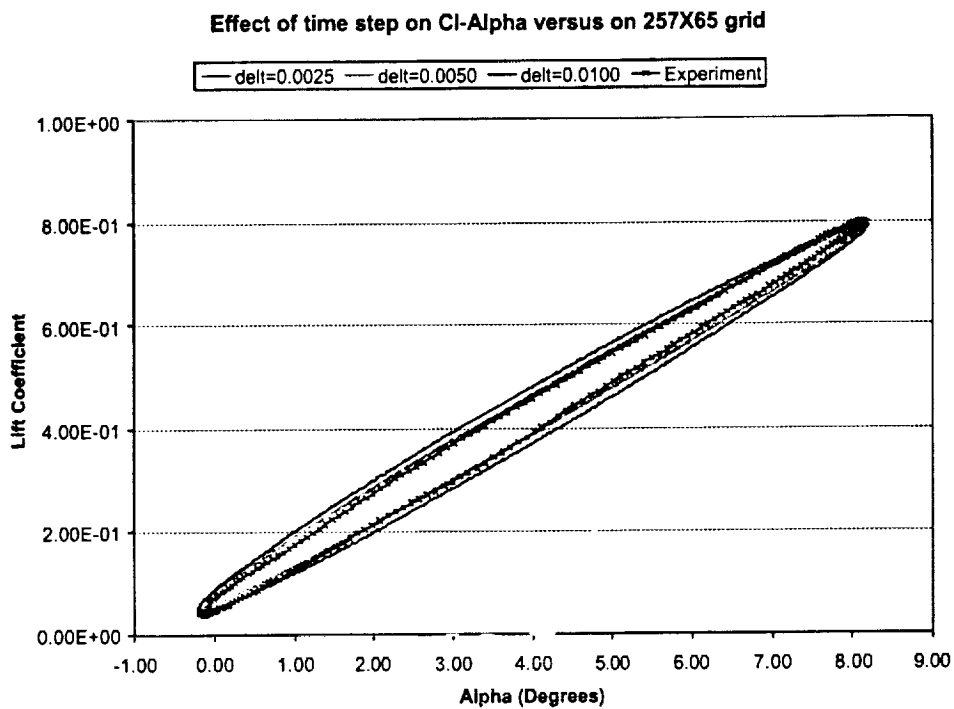
Figure 2 a. Effect of Time Step on Lift Hysteresis Loop

Effect of time step on Cm-Alpha versus on 257X65 grid

| — delt=0.0025 | — delt=0.0050 | — delt=0.0100 | —•— Experiment |
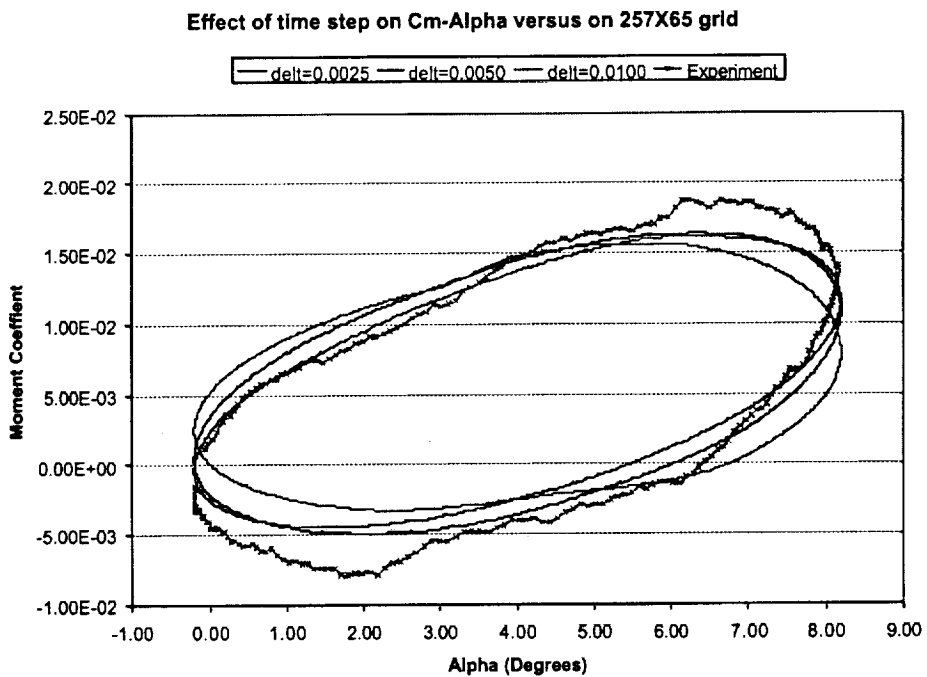
Figure 2 b. Effect of Time Step on Moment Hysteresis Loop

Effect of time step on Cd-Alpha versus on 257X65 grid

— delt=0.0025 — delt=0.0050 — delt=0.0100 — Experiment
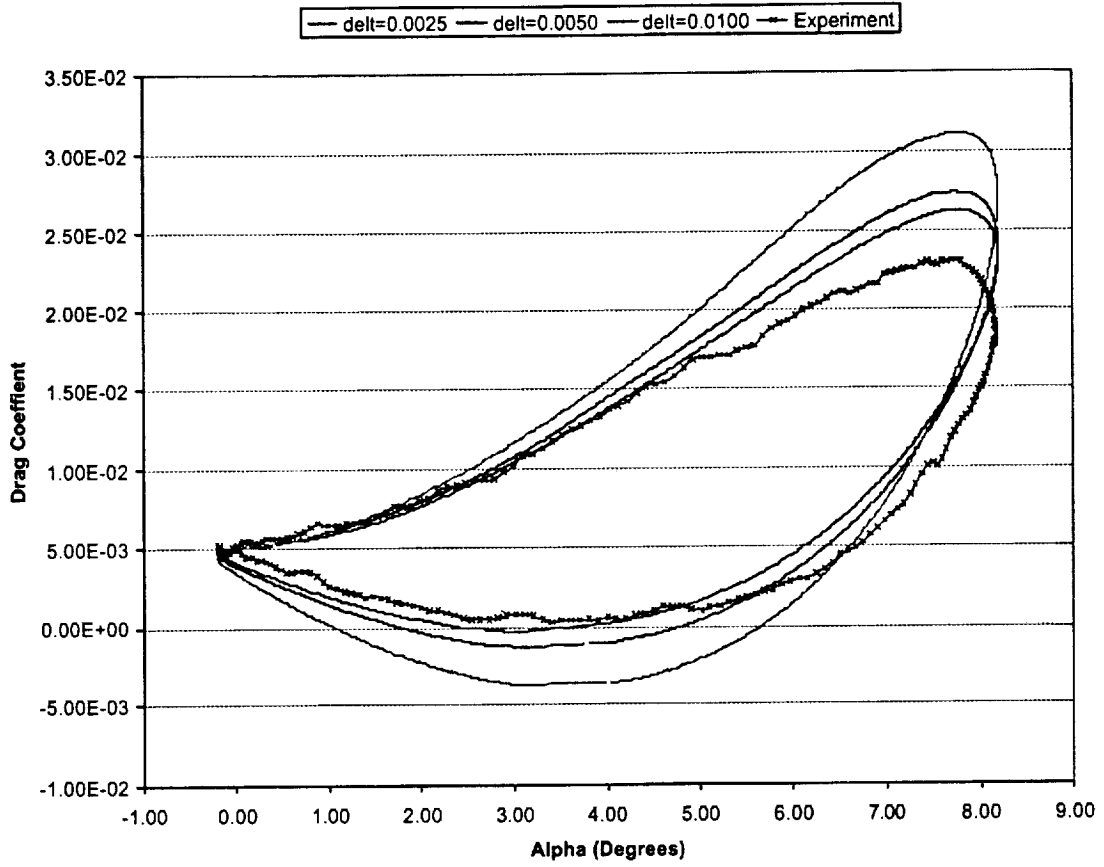
Figure 2 c. Effect of Time Step on Drag Hysteresis Loop
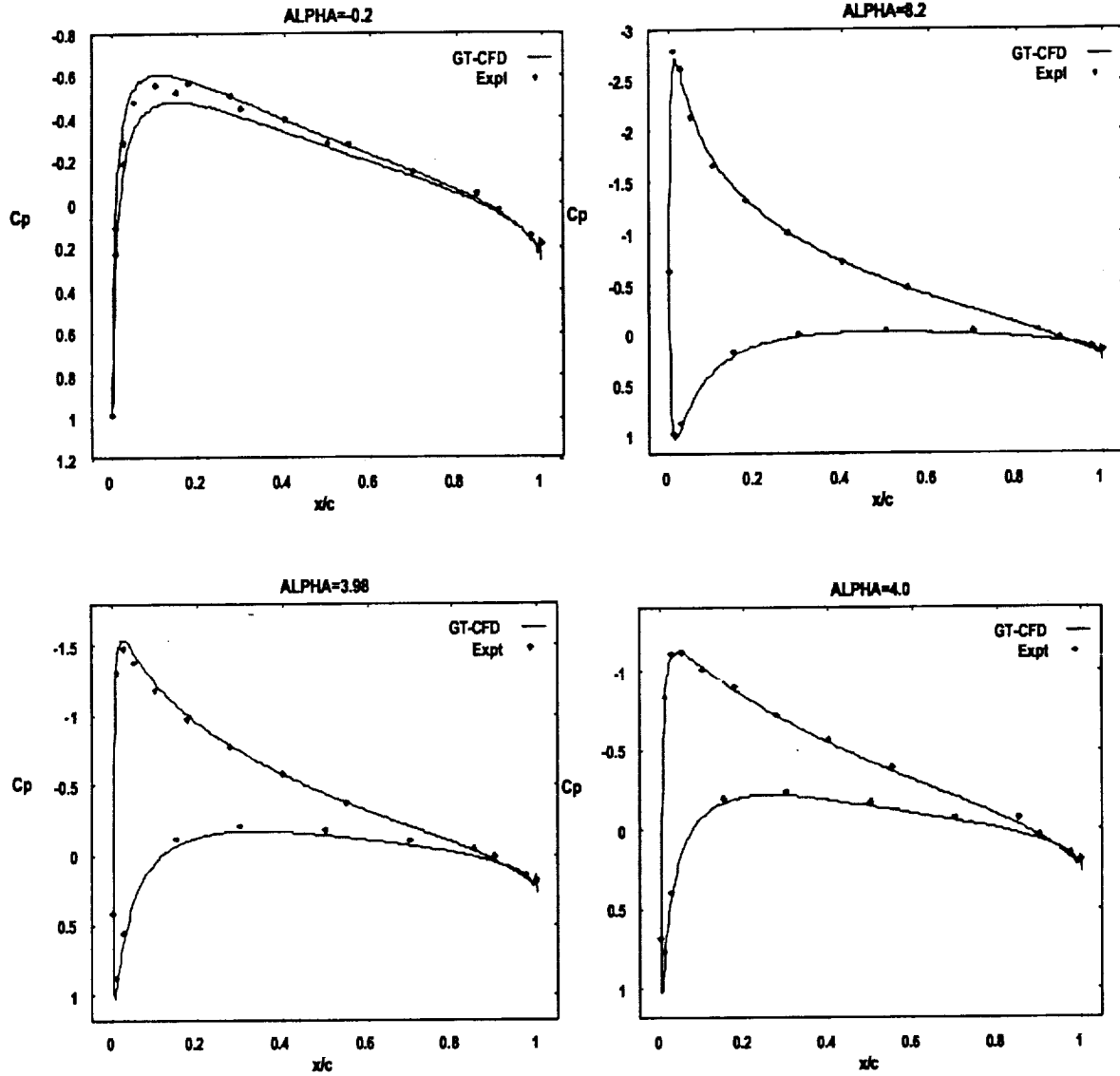
FIGURE 3: Comparison of computed pressure coefficient distribution at several different angle of attacks for the no-stall case.

FIGURE 1.a
Alpha=10.88+4.22cos[wt], k=0.095
Spalart-Allmaras Model, Fully Turbulent
Grid 257X65 and and Δt=0.005
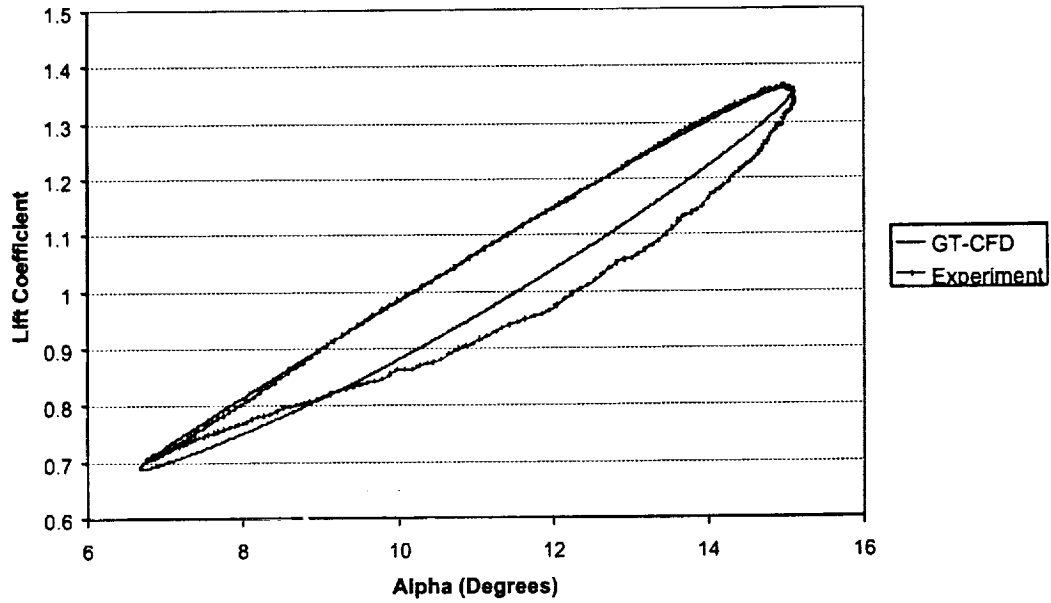
Figure 4 a. Lift Hysteresis Loop using Spalart-Allmaras Model, Light Stall

Alpha=10.88+4.22cos[wt], k=0.095
Fully Turbulent, Baldwin-Lomax Turbulence Model
Grid 257X65 and and Δt=0.005
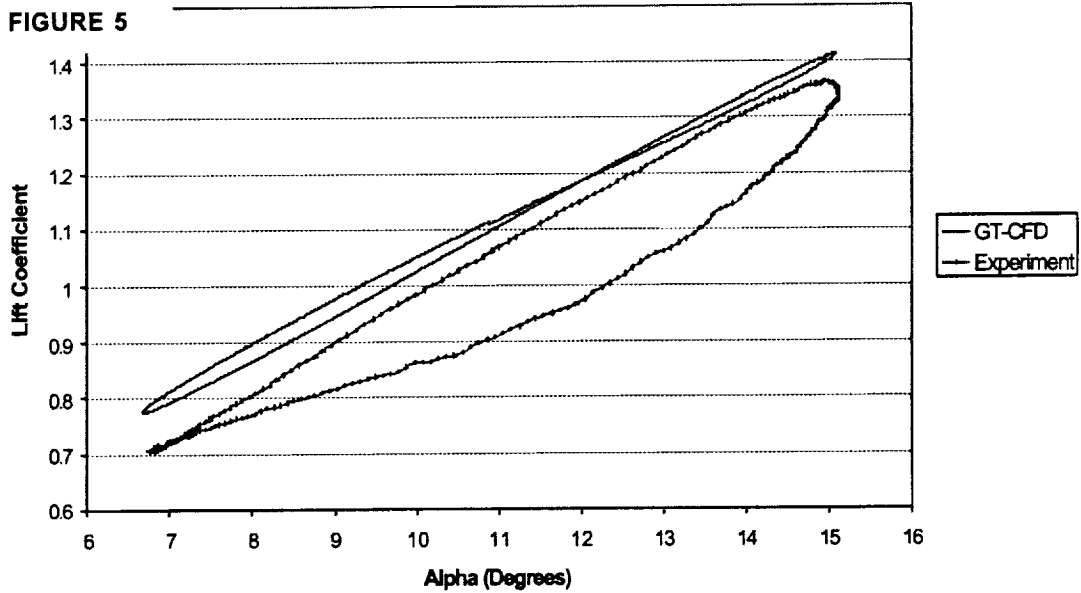
FIGURE 5

Figure 4.b Lift Hysteresis Loop using Baldwin-Lomax Model, Light Stall

20

Alpha=10.88+4.22cos[wt], k=0.095
Spalart-Allmaras Turbulence Model with Michel's Criterion
Grid 257X65 and and Δt=0.005
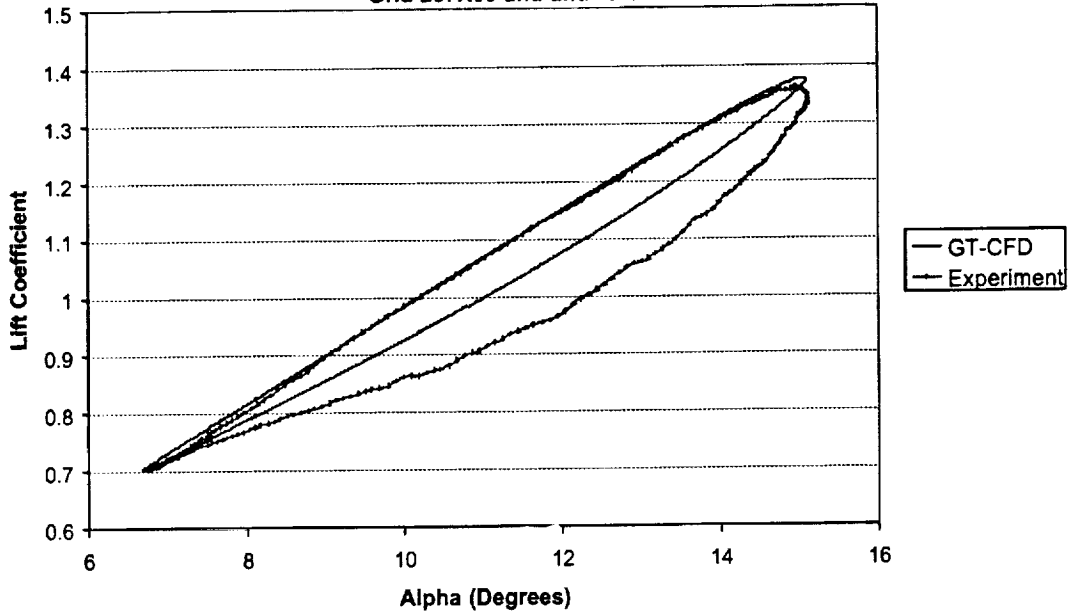
Alpha=10.88+4.22cos[wt], k=0.095
Spallart-Almaras Turbulence Model with Eppler's Criterion
Grid 257X65 and and Δt=0.005
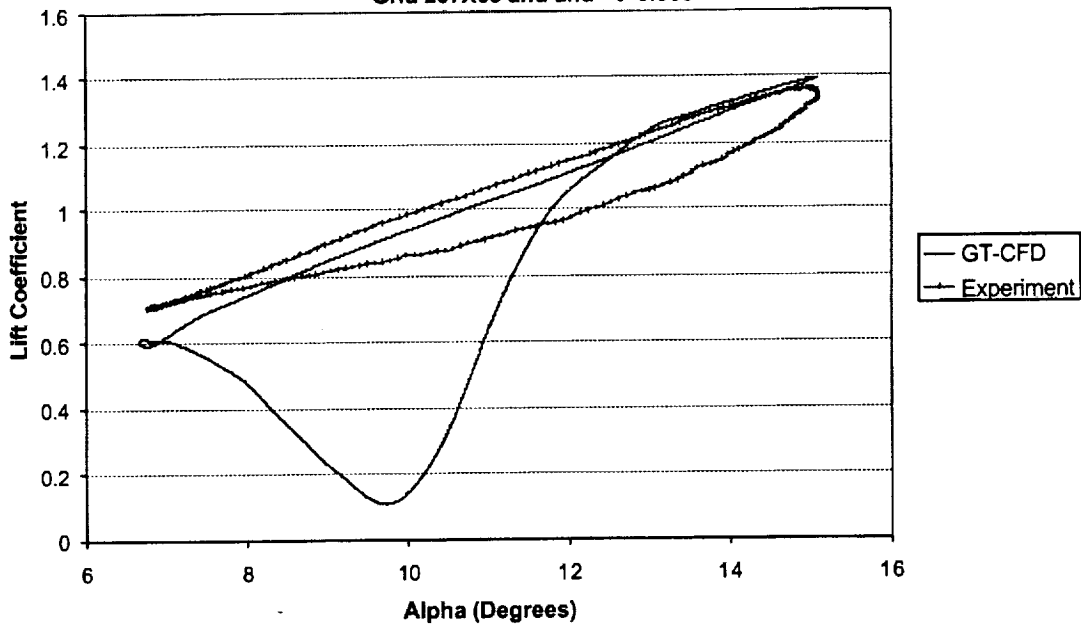
Figure 5. Effects of Transition Model on Lift Hysteresis, Light Stall

APPENDIX B

Dynamic Stall Alleviation using a Deformable Leading Edge Concept - A Numerical Study

AIAA 2000-0520

Dynamic Stall Alleviation using a Deformable Leading Edge Concept - A Numerical Study

Mehmet Sahin, Lakshmi N. Sankar
School of Aerospace Engineering
Georgia Institute of Technology, Atlanta, GA 30332-0150

M. S. Chandrasekhara
Department of Aeronautics and Astronautics
Naval Postgraduate School, Monterey, CA 93943

Chee Tung
Army/NASA Rotorcraft Division
Aerodynamics Directorate (AMRDEC), AMCOM
NASA Ames Research Center, Moffett field, CA 94035-1000

Dynamic Stall Alleviation using a Deformable Leading Edge Concept - A Numerical Study

Mehmet Sahin[*], Lakshmi N. Sankar[**]
School of Aerospace Engineering
Georgia Institute of Technology, Atlanta, GA 30332-0150

M. S. Chandrasekhara[§]
Department of Aeronautics and Astronautics
Naval Postgraduate School, Monterey, CA 93943

Chee Tung[†]
Army/NASA Rotorcraft Division
Aerodynamics Directorate (AMRDEC), AMCOM
NASA Ames Research Center, Moffett field, CA 94035-1000

ABSTRACT

Dynamic stall calculations were carried out for an airfoil with a deformed leading edge shape at a freestream Mach number of 0.3. The surface deformations were done about a baseline NACA 0012 airfoil, effectively increasing the airfoil leading edge radius and thickness at high angles of attack. It was found that the DDLE airfoil had a slightly dynamic stall behavior compared to the baseline NACA 0012 airfoil. In particular, the lift, drag and pitching moment hysteresis loops were milder for the DDLE airfoil compared to the baseline airfoil. It was also found that a static shape that corresponds to the thickest deformed shape performed just as well as the DDLE shape, indicating that the shape itself, and not its time rate of change, was the reason for the improved performance. At higher Mach numbers around 0.4, the DDLE shape exhibited a strong dynamic stall triggered by a shock induced separation, offsetting any benefit from the change in the shape of the airfoil. Additional work is needed on the development of DDLE shapes that will perform well at higher speeds.

INTRODUCTION

Rotary wing aircraft often experience a dynamic stall phenomenon over the retreating blade. Three types of stall - light stall, moderate stall, and strong dynamic stall- have been observed in literature[1]. The strong dynamic stall phenomenon involves three phases. The lift initially increases as the airfoil pitches up, and continues to increase well past the static stall value, $C_{l,max}$. Towards the end of the upstroke, a vortex begins to form near the leading edge and grows in strength. Towards the beginning of the down-stroke, or shortly thereafter, this vortex is shed from the upper surface, creating a rapid loss in the bound circulation and lift. As this vortex rolls downstream over the upper surface, it causes large reductions in local pressure, and high nose down pitching moments. As the airfoil pitches down, one or more weaker vortices are shed from the upper surface, creating additional fluctuations in lift and pitching moment. The flow eventually reattaches at lower angles of attack.

The pitching moments, along with its large variations are transferred to the vehicle through pitch links, or a flex-beam. These components may fail as a result of the high cycle fatigue that develops. These loads also cause vibrations of the fuselage, passenger discomfort, and structural fatigue. Many electronic components and systems (e.g. chips mounted on boards) may experience random failures if the g- loads are high enough, and frequent enough to unseat them.

Many dynamic stall load-alleviation concepts have been proposed in literature. Carr and McAlister[2] proposed a leading edge slat device, which operates much like a slat on a wing and suppresses the leading edge stall. Tuncer and Sankar[3] have numerically studied this using a two-dimensional multi-element dynamic stall solver. A limited number of 3-D calculations have also been done by Bangalore and Sankar[4] to demonstrate that leading edge slats are effective in alleviating dynamic stall. The major drawback of slats is the high drag penalty associated with their use at off-design conditions. A retraction mechanism similar to that found on aircraft will be heavy and costly. For these reasons, this device has not been pursued by the industries.

Another concept that is gaining wide attention is the "synthetic jet" concept. In this approach, mass-less jets generated by flexible cavity walls are used to alter the

---

[*] Graduate Research Assistant, Student Member AIAA.
[**] Regents' professor, Associate Fellow AIAA.
[§] Research Professor and Associate Director, Assoc. Fellow AIAA.
[†] Research Scientist, Associate Fellow AIAA.

boundary layer behavior and prevent stall[5]. If the jets are strong enough, they can act as spoilers destroying lift or as vortex flaps increasing lift. The ability of synthetic jets to eliminate undesirable loads and pitching moments has been computationally studied by Hassan at Boeing Mesa.

A third concept for dynamic stall alleviation is the "Dynamically deforming leading Edge Concept" proposed by Chandrasekhara and Carr[6]. In this approach, the airfoil shape is gradually changed, and the leading edge radius is increased as the airfoil pitches up. Airfoils with large leading edge radii tend to have mild adverse pressure gradients, because the peak local velocities are lower than that for a conventional airfoil. As the airfoil pitches down, and there is no danger of stall, the airfoil returns to its original shape.

In this work, the dynamically deforming leading edge concept (DDLE) is computationally studied. A two-dimensional compressible Navier-Stokes solver is used. The baseline shape is a NACA 0012 airfoil, which is deformed according to the schedule prescribed in Ref. 6. It is demonstrated that the dynamic stall process is indeed alleviated by the use of the deforming leading edge shape. This is done through a comparison of the surface pressure distributions and load hysteresis loops for the baseline NACA 0012 airfoil and the DDLE airfoil.

MATHEMATICAL AND NUMERICAL

FORMULATION

A two-dimensional compressible Navier-Stokes solver is used in this study. This solver uses a curvilinear body-fitted grid, that will pitch up or down with the airfoil. The scheme is second order or fourth order accurate in space, and is first order accurate in time. A two-layer eddy viscosity model is used to account for the effects of turbulence. Wu and Sankar describe the mathematical formulation behind this analysis, and applications of this solver[7]. Three-dimensional versions of this solver that can model oscillating wings[8] and rotors also exist[9].

At each time step, the airfoil surface and the surrounding grid are distorted using the schedule provided in Ref. 6. For the given discrete set of airfoil surface points, the Gram-Schmidt orthonormalization process described in Ref. 10 is used to generate a smooth function defining the airfoil geometry. The dynamic grid adaptation used here is similar to the work of Batina[11]. The grid around the body is considered to be a system of interconnected springs. This system is constructed by representing a grid line joining two successive grid points by a tension spring. Whenever the airfoil boundary moves, all the grid nodes must be adjusted so that the nodes are force-free.

The value of spring stiffness determines how much a node will move and can be specified in different ways. In this work, the spring stiffness is assumed inversely

proportional to length of distance between two successive grid points and given as

$$k_{m,k} = 1.0 \left[(x_{m,k} - x_{i,j})^2 + (y_{m,k} - y_{i,j})^2 \right]^{p/2} \quad (1)$$

Where p is a parameter used to control the stiffness of the spring (chosen as 5). The grid deformation due to boundary geometry change is solved explicitly by using several Jacobi iterations.

$$\Delta x_{i,j}^{n+1} = \sum k_{m,k} \Delta x_{m,k}^n / \sum k_{m,k} \quad (2.a)$$

$$\Delta y_{i,j}^{n+1} = \sum k_{m,k} \Delta y_{m,k}^n / \sum k_{m,k} \quad (2.b)$$

where the subscripts m,k indicate the grid points which are connected to point i, j. The new location of the interior nodes are determined by

$$x_{i,j}^{n+1} = x_{i,j}^n + \Delta x_{i,j}^{n+1} \quad (3.a)$$

$$y_{i,j}^{n+1} = y_{i,j}^n + \Delta y_{i,j}^{n+1} \quad (3.b)$$

Figure 1 shows the leading edge shapes used. Figure 2 shows the amplitude of deformation, as a function of time. The angle of attack of the airfoil is also shown. Figure 3 shows the body-fitted grid in the vicinity of the leading edge at several time levels. Good clustering of the grid, and near-orthogonality are evident.

RESULTS AND DISCUSSION

Dynamic stall calculations were done for the baseline airfoil, and the DDLE airfoil. The reduced frequency k= ωc/2V∞ is 0.05, where ω is the circular frequency, c is the airfoil chord, and V∞ is the freestream velocity. The airfoil pitching motion is described by:

$$\alpha = 10° + 10° \cos(\omega t) \quad (4)$$

Four sets of calculations were done: (i) NACA 0012 airfoil at a freestream Mach number M=0.3, (ii) DDLE airfoil at M=0.3, with the variation is shape described in Ref. 6. (iii) the DDLE airfoil with a fixed "thickest" shape at M=0.3, and (iv) DDLE airfoil at M=0.4. The Reynolds number in all these cases was 1,065,000.

The present calculations assume that the flow is turbulent everywhere. At the Reynolds number of the experiment, there is a large laminar region present, and the transition point moves with the angle of attack. The transition location dramatically affects the onset of separation, and ultimately, the stall. A sophisticated

transition model is required to be developed for pressure gradient flows for use here. In its absence, a one-to-one comparison between the present theory and experiments is not possible at this time. Nevertheless, the qualitative differences between the NACA 0012 and the DDLE airfoil behavior are in accord with what was observed in the experiments.

NACA 0012 vs. DDLE Airfoil:

Figure 4 shows the streamlines, and the vorticity contours around the oscillating NACA 0012 and the DDLE airfoils, at selected instances in time. The surface pressure distribution is also shown at these time levels. During the upstroke, up to an angle of attack of 18 degrees or so, the flow field remains attached over both the airfoils. Some increased thickening of the boundary layer is evident on the upper surface as the angle of attack increases.

Around 19.43 degrees during the upstroke, the NACA 0012 airfoil develops a strong leading edge vortex, seen as a "bump" in the surface pressure distribution in figure 4b. The streamlines show considerable amount of separation and recirculation on the upper surface. In contrast, for the DDLE airfoil, even though the entire upper surface boundary layer has separated, the thickness of the separation bubble is smaller. There is also no evidence of a leading edge vortex in the vorticity contours, or the surface pressure distribution.

At the end of the upper stroke, at $\alpha = 20$ degrees, the streamline plot and the vorticty contours both indicate that leading edge vortex has already been shed for the NACA 0012 airfoil. There is a considerable loss in lift, as evidenced by the collapse of the suction peak. The DDLE airfoil, in contrast, is just beginning the dynamic stall process. It thus appears that the dynamic stall process is delayed by half a degree or so, as a result of the deforming leading edge action.

During the downstroke, as shown by the pressure, vorticity and streamline plots at $\alpha = 19.66, 15.31$ degrees, the flow over the NACA 0012 airfoil and that over the DDLE airfoil are completely different. A second vortex forms and sheds over the NACA 0012 airfoil. The DDLE airfoil, on the other hand experiences a gradual attachment of the boundary layer, with the separation point migrating from the leading edge to the trailing edge. It thus appears that the DDLE action dramatically improves the airfoil performance during the downstroke. By the time the airfoil reaches an angle of attack of 10 degrees, the flow field has attached and is well behaved for both the airfoils.

Figure 5 shows the load hysteresis loops for the DDLE airfoil and the baseline NACA 0012 airfoil. As expected, for the NACA 0012 airfoil, the lift drops abruptly twice during the downstroke. The pitching moment distribution also shows two large negative peaks, attributable to the large levels of suction that develop near the airfoil trailing edge as the vortex moves over the airfoil. The DDLE airfoil, on the other hand, shows just a single

drop in the lift and a single peak in the pitching moment. These abrupt variations in the lift and pitching moment directly translate into vibratory loads on the fuselage, and contribute to pitch link fatigue. It is clear that the DDLE airfoil is preferred over the NACA 0012 airfoil from these two (vibratory load and fatigue) considerations.

DDLE Airfoil with a Fixed Shape:

Given the benefits of the DDLE airfoil, the following question arises. How much of the benefit is attributable to the changes to the shape, and how much is attributable to the surface dynamics, i.e. the rate of change of slope? To answer this question, the DDLE dynamics stall calculations were repeated, with a fixed shape that corresponds to "Shape 8.5" in Ref. 6. This corresponds to the largest leading edge radius, and the bluntest leading edge. It was found that the streamline, vorticity contour and surface pressure variations with angle of attack behavior were identical to the DDLE shape. The integrated loads, as shown in figure 6, were identical for the DDLE shape (where the airfoil shape continually changes) and the fixed 8.5 shape.

Thus it appears that much of the benefits of the DDLE airfoil were attributable to just the increased leading edge radius, and not the rate of change. A passive well-designed shape should be able to experience a milder dynamic stall for the conditions studied, than the NACA 0012 airfoil.

On the other hand, a blunter, thicker passive airfoil shape may have undesirable high-speed characteristics. The blunter leading edge may lead to high locally supersonic velocities and premature formation of shocks on the advancing side. The DDLE shape is thus a compromise between the baseline airfoil that may have good high-speed characteristics, and a thicker, blunter airfoil that has good dynamic stall characteristics.

Behavior of the DDLE Airfoil at Higher Mach Numbers:

To determine the behavior of the DDLE airfoil (with a dynamically changing shape) at higher Mach numbers, the previous calculations were repeated at M=0.4. Form a visualization of the streamline and vorticity contours (not shown here, for brevity), the following phenomena were observed. The flow separated immediately downstream of the shock wave. During the upstroke, around 15 degrees or so, a weak shock formed on the upper surface. The shock induced separation process, and the gradual upstream migration of the turbulent flow separation point, combined to trigger a dynamic stall event during the upstroke. The flow attempted to recover during the downstroke, but a second vortex quickly formed and shed. The lift, drag and pitching moment variations are shown in figure 7. It appears that the DDLE airfoil, with the surface shape variation schedule given in Ref. 6, was not effective in mitigating the dynamic stall process at this higher Mach

number. Additional studies are needed to arrive at DDLE shapes that behave well at higher Mach numbers.

CONCLUDING REMARKS

Dynamic stall calculations have been carried out for a dynamically deforming leading edge airfoil at two Mach numbers – 0.3 and 0.4. At the lower Mach number, it is found that the DDLE airfoil has better dynamic stall characteristics over a conventional NACA 0012 airfoil. This improvement was found attributable to the shape itself, and not the rate at which the shape was changed. At the higher Mach number, the DDLE shape experienced a shock-induced stall during the upstroke, and its dynamic stall characteristics were quite similar to that of the NACA 0012 airfoil at low Mach numbers. Additional studies are needed to develop deforming leading edge shapes that perform satisfactorily at high Mach numbers.

These results are in qualitative agreement with those described in Ref. 6. Since the flow in that study was transitional in nature, the peak suction developed was smaller than found in the present study. Further, both the shape 8-5 airfoil and the adapting airfoil flows were dynamic stall vortex free. A complete modeling of the transition behavior of the flow may enable better agreement between the present theory and experiments.

REFERENCES

1. Carr, L. W., McAlister, K. W. and McCroskey, W. J., "Analysis of the development of Dynamic Stall from oscillating Airfoil Experiments," NASA TN-D-838270, 1977.
2. Carr, L. W. and McAlister, K. W., "The Effects of Leading Edge Slat on the Dynamic Stall of an oscillating Airfoil," AIAA Paper 85-2533, October 1983.
3. Tuncer, I. And Sankar, L. N., "Unsteady Aerodynamic Characteristics of a Dual-Element Airfoil," Journal of Aircraft, Vol. 31, No. 3, May-June 1994.
4. Bangalore, A. and Sankar, L. N., "Numerical Analysis of Aerodynamic Performance of Rotors with Leading Edge Slats,' Journal of Computational Mechanics, Vol. 17, pp. 335-342,1996.
5. Seifert, A., Bachar, T., Koss, D., Shepshelovich, M. and Wygnanski, I., "Oscillatory Blowing - A Tool to delay Boundary Layer Separation," AIAA Journal, Vol. 31, No. 11, November 1993, pp. 2052-2060.
6. Chandrasekhara, M. S. and Carr, L. W., "Unsteady stall Control using Dynamically Deforming Airfoils," AIAA Journal, Vol. 36, No. 10, 1998.
7. Wu, Jiunn-Chi, Huff, D. and Sankar, L.N., "Evaluation of Three Turbulence Models in Static Airloads-and Dynamic Stall Predictions," Journal of Aircraft, Vol. 27, No. 4, April 1990, pp382-384.
8. Sankar, L. N., Malone, J. B. and Schuster, D., "Euler Solutions for Transonic Flow past a Fighter Wing," Journal of Aircraft, Vol. 24, NO. 1, pp. 10-1 6, 1987.
9. Bangalore, A and Sankar, L. N., "Forward Flight Analysis of Slatted rotors using Navier-Stokes methods," Journal of Aircraft, Vol. 34, No. 1, January-February 1997, pp. 80-86.
10. Chang I-C., Torres F. J. and Tung C., "Geometric Analysis of Wing Sections", NASA-TM-110346, 1995.
11. Batina J.T. "Unsteady Euler Airfoil Solutions Using Unstructured Dynamic Meshes", AIAA Paper 89-0115.
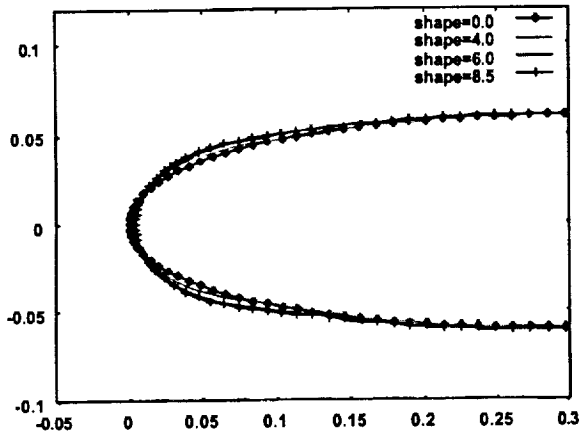
Figure.1.DDLE Airfoil shape profiles
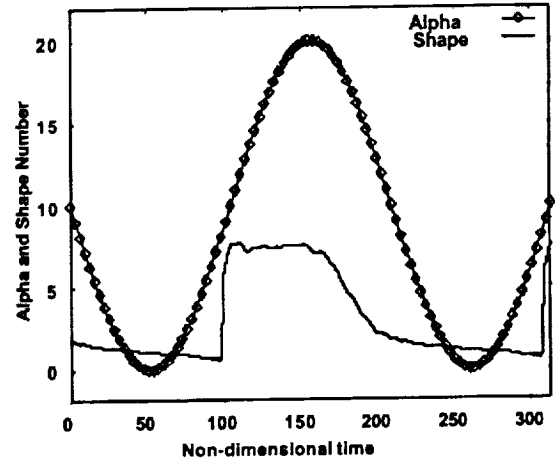
Figure.2. DDLE Shape and Angle of Attach History (V1V05SO-8D5)
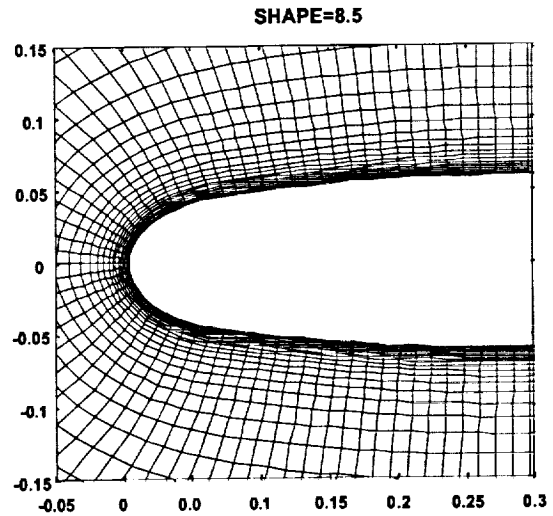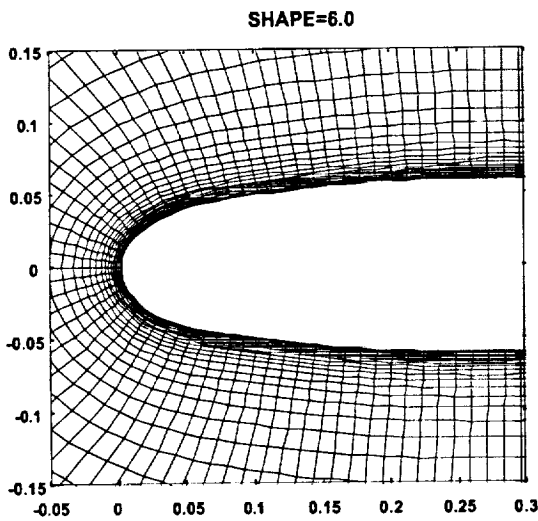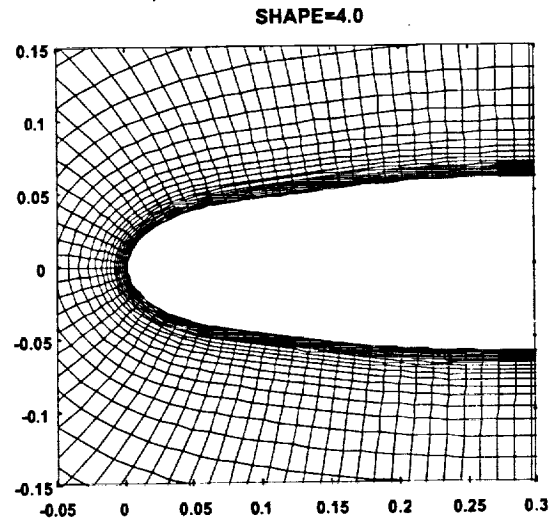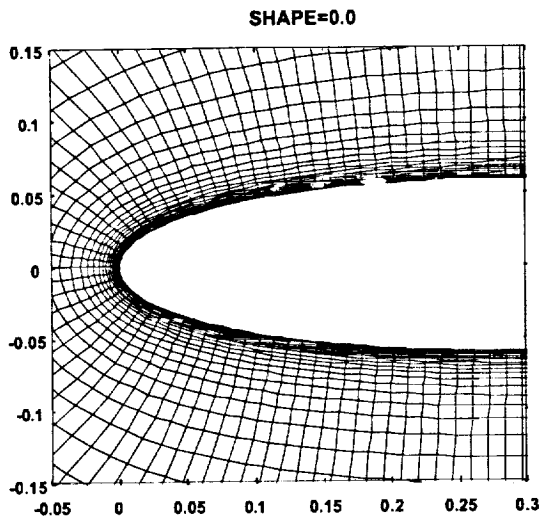
Figure.3. Leading edge grid deformation for DDLE airfoil shape profiles.

28
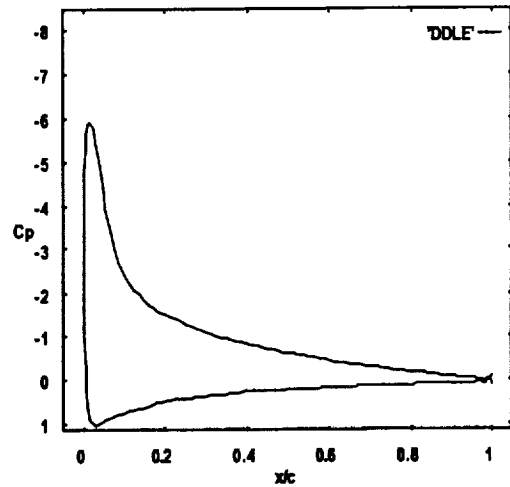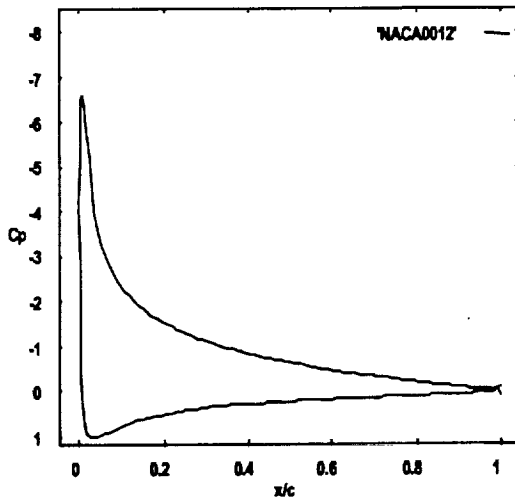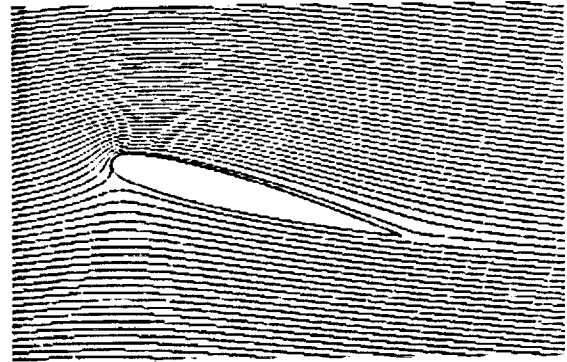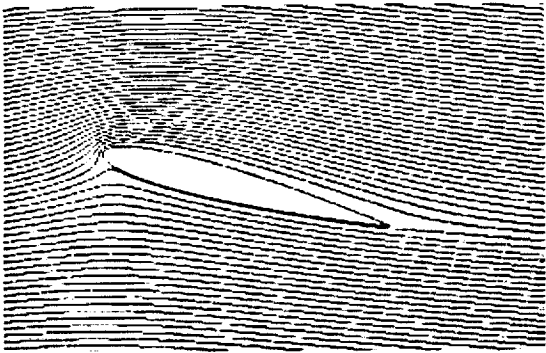
Figure.4.a.1: Streamlines, vorticity contours and surface pressure coefficient over the NACA0012 airfoil at α=14.62⁰.

Figure.4.a.2: Streamlines, vorticity contours and surface pressure coefficient over the DDLE airfoil at α=14.62⁰.
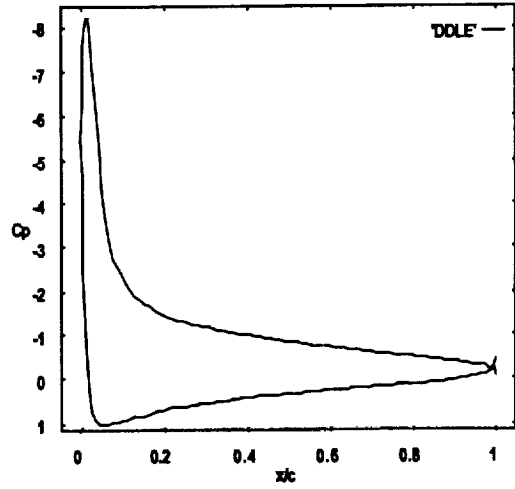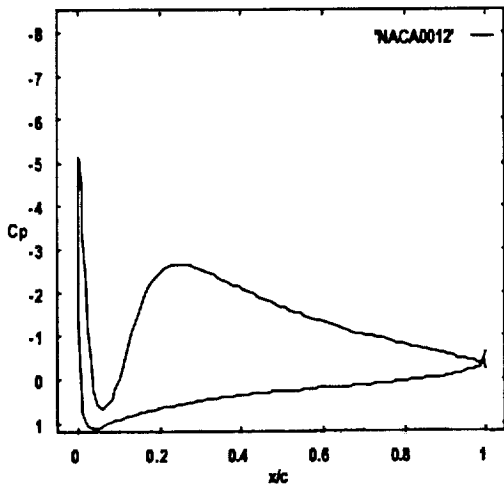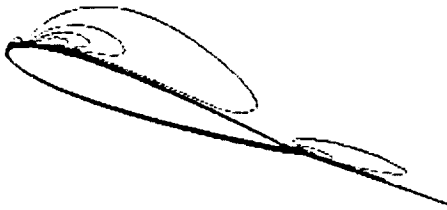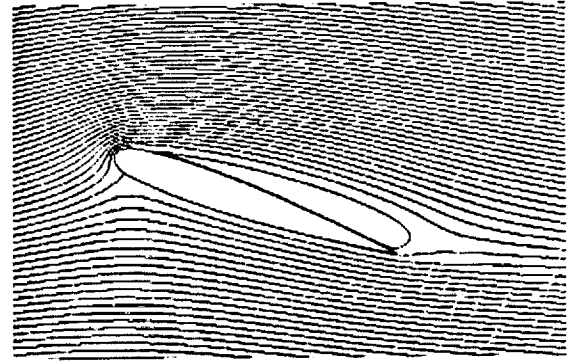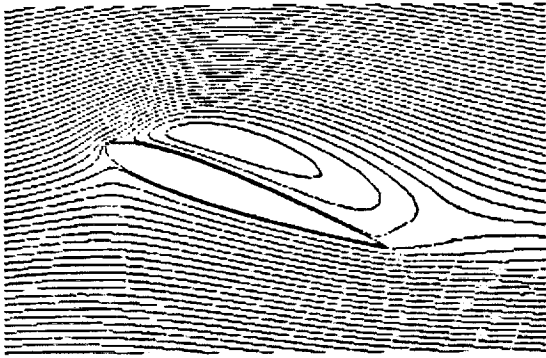
Figure.4.b.1: Streamlines, vorticity contours and surface pressure coefficient over the NACA0012 airfoil at $\alpha=19.43^{0}$.

Figure.4.b.2: Streamlines, vorticity contours and surface pressure coefficient over the DDLE airfoil at $\alpha=19.43^{0}$.
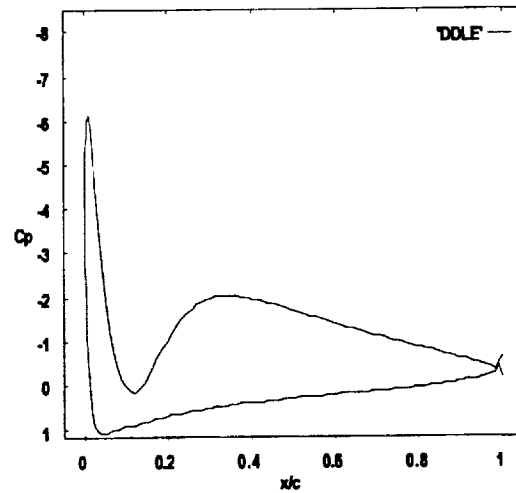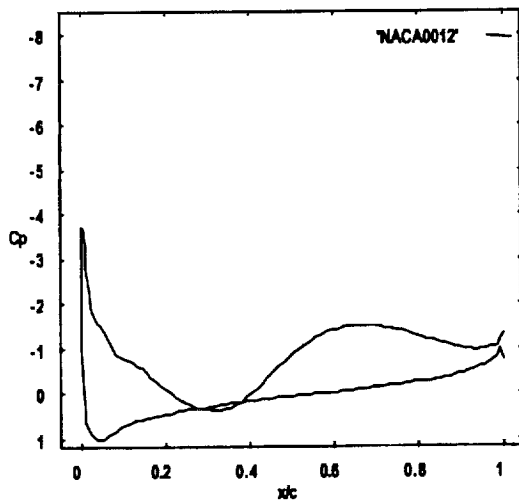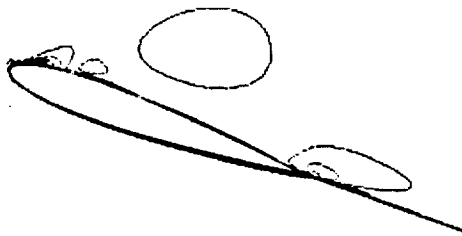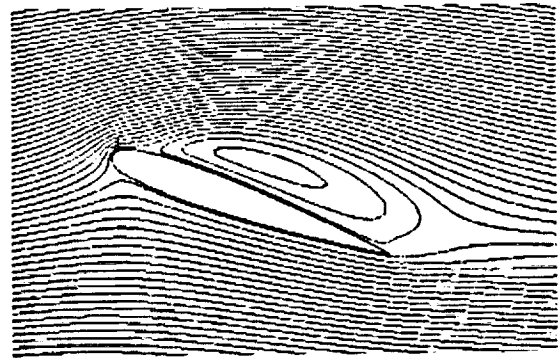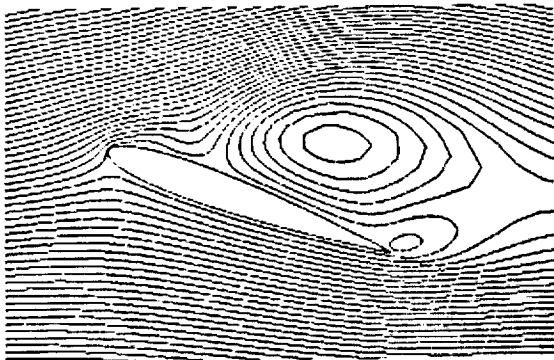
Figure.4.c.1: Streamlines, vorticity contours and surface pressure coefficient over the NACA0012 airfoil at α =20.00^0.

Figure.4.c.2: Streamlines, vorticity contours and surface pressure coefficient over the DDLE airfoil at α = 20.00^0.
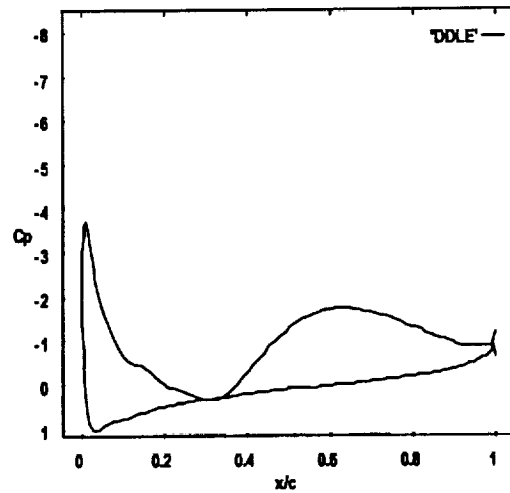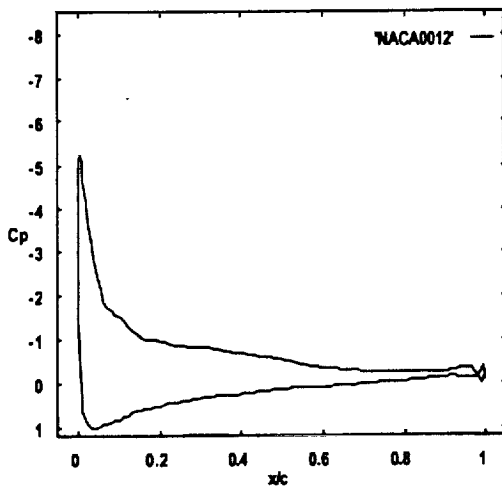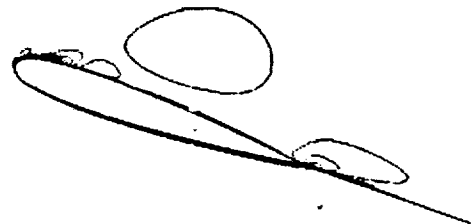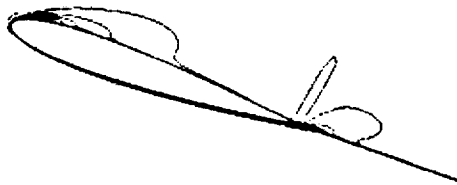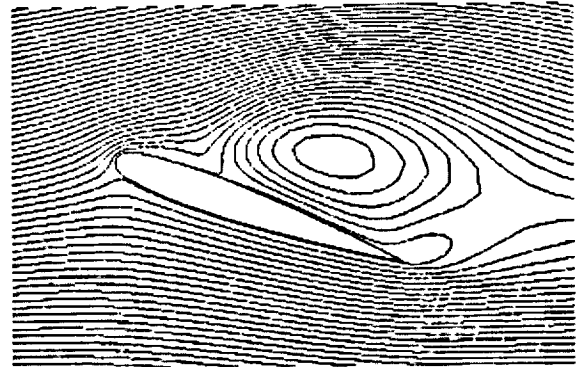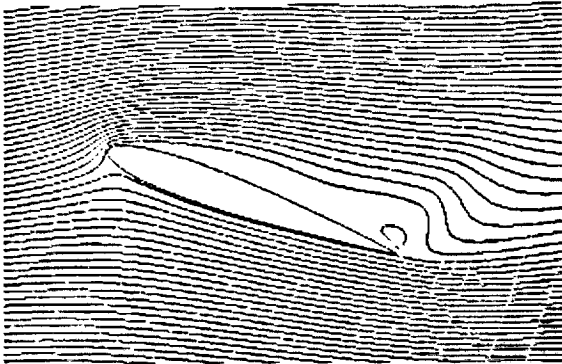
Figure.4.d.1: Streamlines, vorticity contours and surface pressure coefficient over the NACA0012 airfoil at α=19.66^0.

Figure.4.d.2: Streamlines, vorticity contours and surface pressure coefficient over the DDLE airfoil at α=19.66^0.
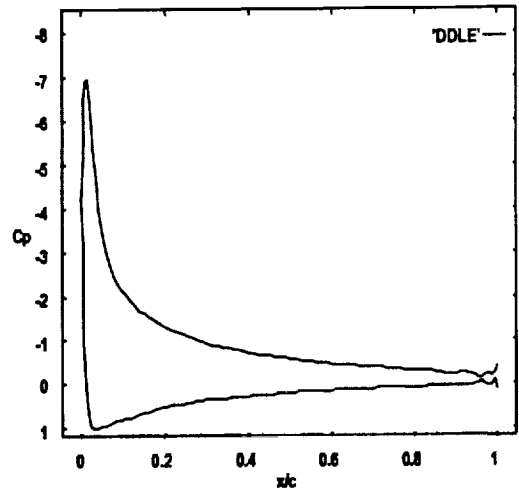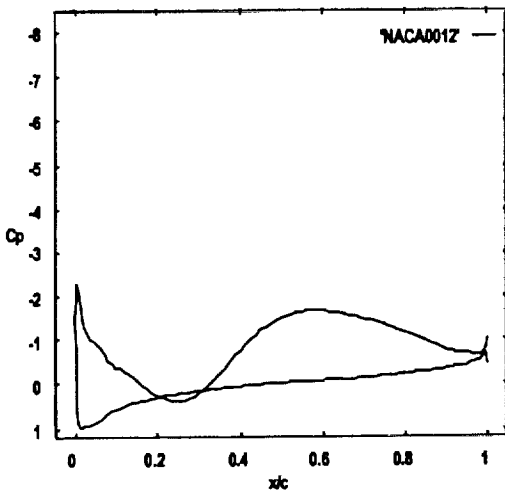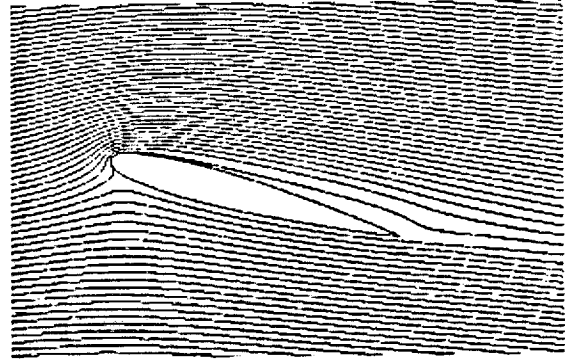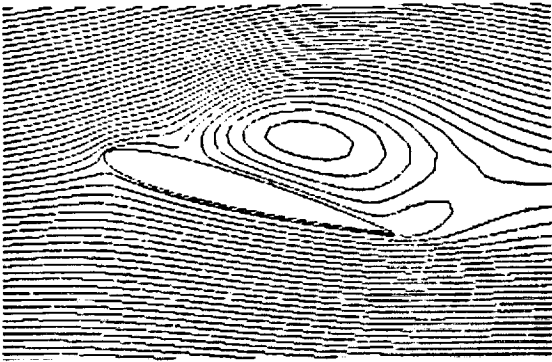
Figure.4.e.1: Streamlines, vorticity contours and surface pressure coefficient over the NACA0012 airfoil at α=15.31^0.

Figure.4.e.2: Streamlines, vorticity contours and surface pressure coefficient over the DDLE airfoil at α=15.31^0.
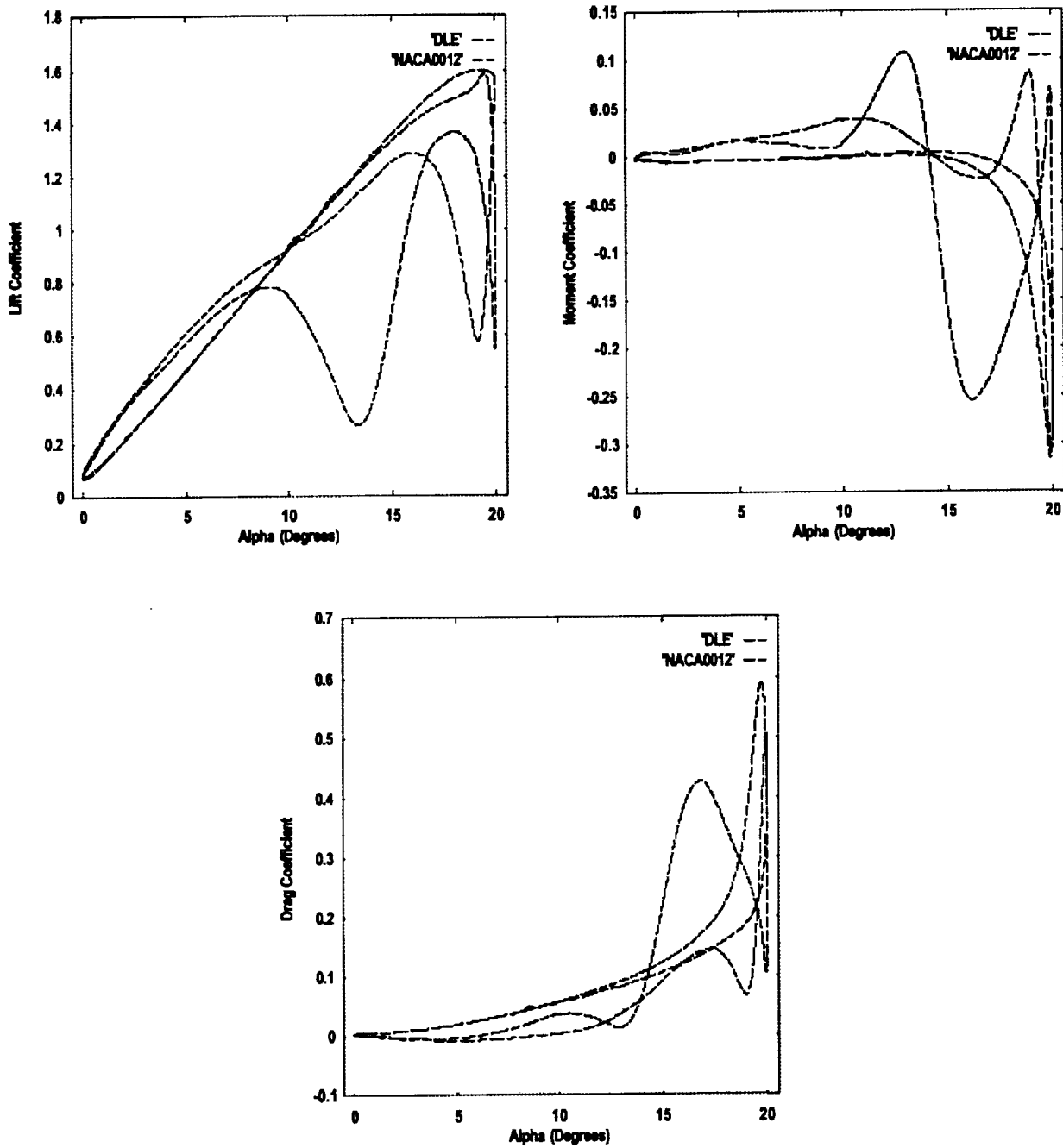
Figure 5. Lift, Drag and Pitching Moment Hysteresis Loops for the NACA 0012 and the DDLE Airfoils.
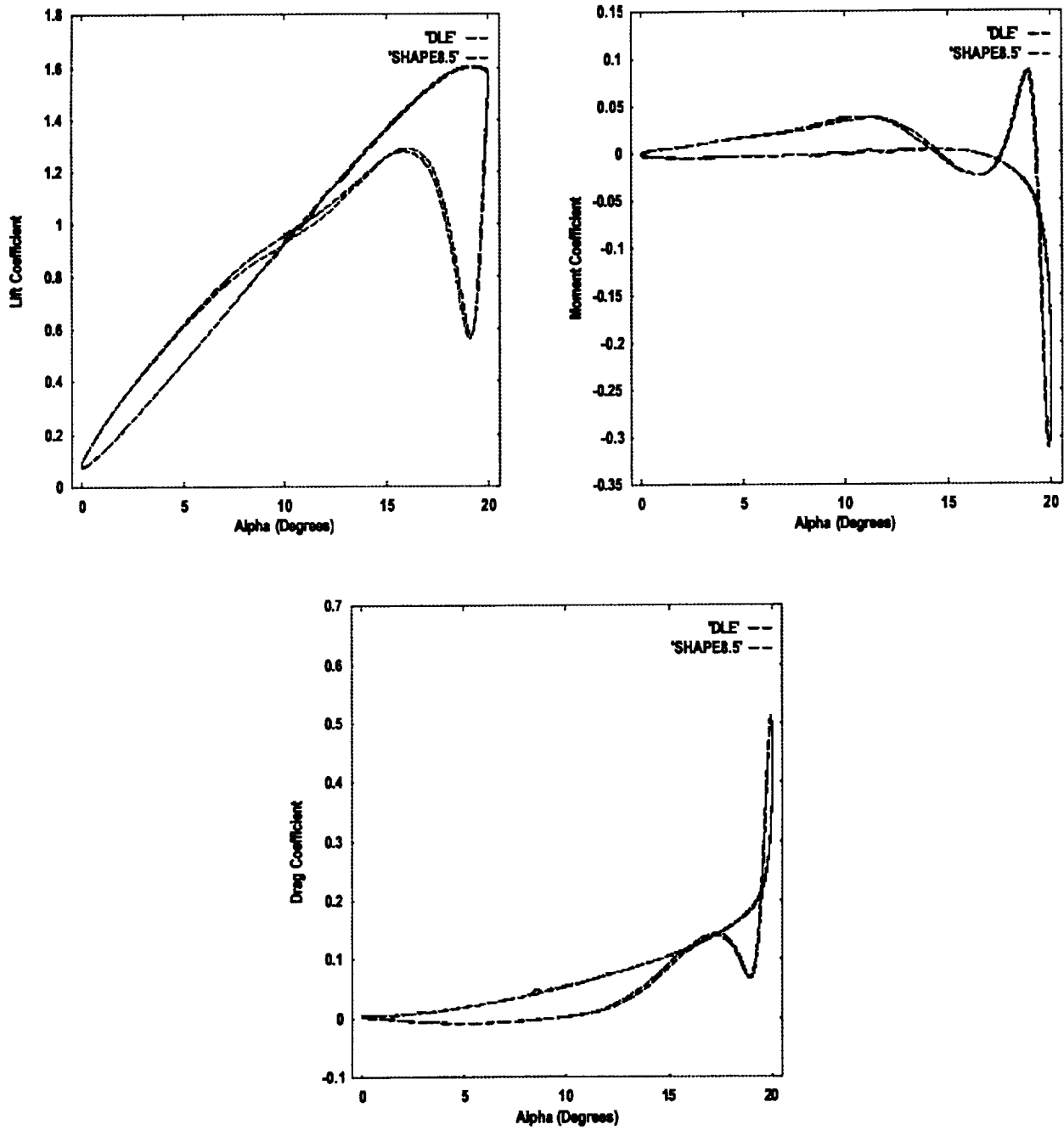
Figure 6. Comparison of the Load Hysteresis Characteristics between the DDLE Airfoil and the Fixed 8.5 Shape.
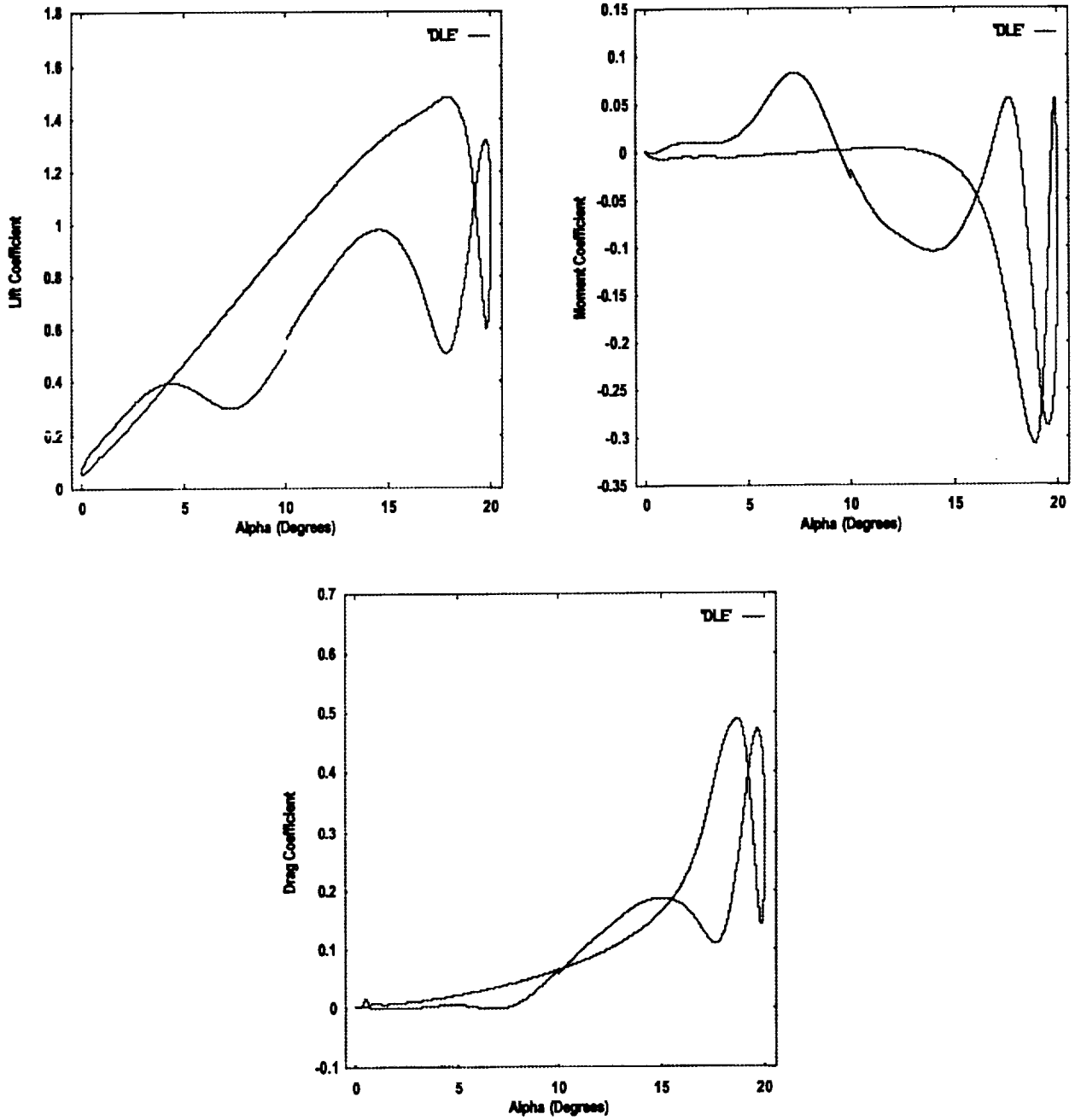
Figure 7. Dynamic Stall Load Hsyeteresis Characteristics of the DDLE Airfoil at M=0.4.

APPENDIX C

DYNAMIC STALL CHARACTERISTICS OF DROOPED LEADING EDGE AIRFOILS

INTRODUCTION

A number of passive and active techniques for the alleviation of dynamic stall have been proposed and explored by researchers. The primary goal of this research work was to evaluate the effectiveness of drooped leading edge in delaying and suppressing stall. This is achieved by making the flow pass smoothly around the airfoil in the case of an airfoil with drooped leading edge. Two airfoils were selected for this study, the base line VR-12 having a two-dimensional planform of 10cm (chord) by 21 cm (span) and the drooped VR-2513 derived from VR-12 by rotating the leading edge region by a droop angle of 13°. This particular configuration has been studied in a water tunnel by McAlister et al. Numerical simulations have also been attempted by Wang et al using an incompressible Navier-Stokes solver (ZETA). McAlister's work and Wang's work were carried out at low or zero mach numbers. McAlister et al studied the effectiveness of the deformable leading edge (DLE) at a low reynolds number of 200,000 and a reduced frequency, k=0.1. The purpose of this study (DSS2, Sankar et al) was to compare the dynamic stall characteristics of the drooped leading edge airfoil (VR-2513) and the standard base line airfoil (VR-12) at a compressible mach number M=0.2 and a relatively high Reynolds number (Re=2,000,000).

The phenomenon of flow separation above a certain critical angle of attack leading to loss of lift is called 'Static stall'. The dynamic motion of an airfoil fundamentally alters the stall process leading to large values of lift prior to the onset of stall and is called 'Dynamic stall'. The complex events associated with the dynamic stall are flow separation leading to shedding of primary vortex from leading edge region and relatively weaker secondary vortex shed near the trailing edge region. This leads to two important consequences - large hysteresis of lift, drag and moment due to lag, and asymmetry of the response of airloads and unfavorable aerodynamic damping.

McCroskey has categorized four distinct dynamic stall regimes. The categorization is a function of reduced frequency, Mach number and the maximum incidence angle attained by the airfoil. In the *no stall regime* the maximum angle of attack is less than the static stall angle. There is no separation and no hysteresis loops. When α_{max} increases up to or slightly over the static stall angle, there is small amount of separation and hysteresis. This is called the *stall onset regime*. In the next regime, termed the *light dynamic stall regime*, α_{max} is one or two degrees beyond the stage of stall onset causing a distinct hysteresis and moment stall. Intensification of moment stall, large amount of hysteresis and vortex shedding characterize the *deep stall regime*.

To investigate the static and dynamic characteristics of the drooped leading edge, an incompressible Navier-stokes code (named DSS2) was employed. To achieve a comprehensive investigation, calculations were carried out in the following three dynamic stall flow regimes:

(a) No Stall/ Stall-onset regime $\qquad$ $\alpha = 11.00° \pm 4.00°\cos(\omega t)$

(b) Moderate stall regime / light stall $\qquad$ $\alpha = 14.00° \pm 4.00°\cos(\omega t)$

(c) Deep stall regime $\qquad$ $\alpha = 15.00° \pm 10.00°\cos(\omega t)$

The calculations were carried out at the following flow conditions:

Reynolds number (Re)=2,000,000

Mach number (M)= 0.2

Reduced Frequency (K)=0.1

Turbulence Model: Baldwin–Lomax model, Fully Turbulent conditions.

Both Spallart–Allmaras model simulation and a simulation based on Baldwin-Lomax models was done. There were only slight differences in the predictions with these models for the cases investigated. Because the Baldwin-Lomax model was computationally cheaper, detailed diagnostic studies of the flow were done using this model.

RESULTS AND DISCUSSION

Figures 1-9 give the surface pressures, vorticity contours and streamline plots (in a rotating frame) for the three cases (three flow regimes). The angle of attacks (α) were chosen near maximum angle of attack ($\alpha_{max} \pm 1$) to see how the flow behaves near α_{max}.

The following conclusions can be drawn.

a) The adverse pressure gradient (dp/dx) is milder for the drooped leading edge airfoil (VR-2513) then for VR-12.

b) Suction peak (Cp peak) is lower for the drooped leading edge airfoil (VR-2513).

c) Separated flow size is in general smaller for the drooped leading edge airfoil (VR-2513).

d) Vortex strength is comparatively lower for the drooped leading edge airfoil (VR-2513).

Figures 10-12 show the corresponding hysteresis loops, C_L Vs α, C_D Vs α and C_M Vs α. The following conclusions can be drawn.

d) At low angles of attack ($\alpha = 11°\pm4°$), both the airfoils experienced attached flow. The maximum lift $C_{l,max}$, the maximum drag $C_{d,max}$ as well as the maximum nose-down pitching moments were comparable for the two airfoils.

e) At moderate angles of attack, ($\alpha = 14°\pm4°$), the baseline airfoil experienced a mild stall, with an attendant rise in drag and nose-down pitching moment. The drooped leading airfoil did not stall at all. An examination of the flow field indicated that this desirable behavior is a consequence of the milder adverse pressure gradient in the nose region of the drooped leading edge airfoil. The conventional airfoil has a high suction peak, and a rather steep adverse pressure gradient and is more prone to stall.

f) At higher angles of attack, ($\alpha = 15°\pm10°$), both the airfoils experienced dynamic stall. Even under such a severe condition, dropped airfoil had more desirable characteristics (lower $C_{d,max}$ lower maximum nose-down pitching moments), although the $C_l - \alpha$ hysteresis loop was some what larger for the VR-12 airfoil.

CONCLUDING REMARKS

A 2-D dynamic stall solver has been improved with the addition of a new turbulence model and a transition model. Several validation studies have done, prior to the application of this solver to two promising dynamic stall alleviation concepts: a drooped leading edge airfoil, and a dynamically deformed leading edge airfoil. Both concepts showed promising improvements in the dynamic stall characteristics compared to the baseline airfoil. Additional studies over a wider range of Mach numbers and reduced frequencies are needed to further evaluate these two concepts.
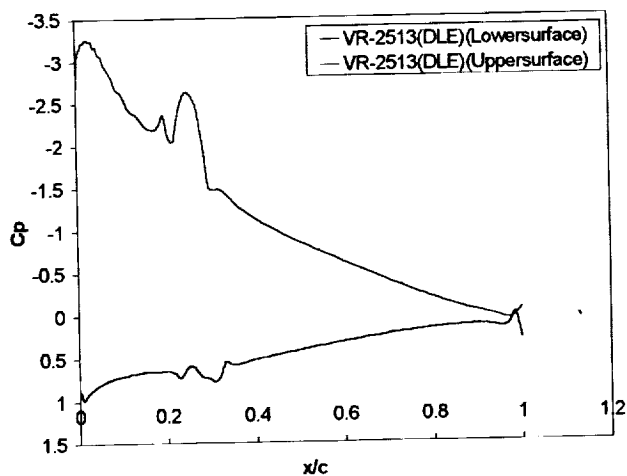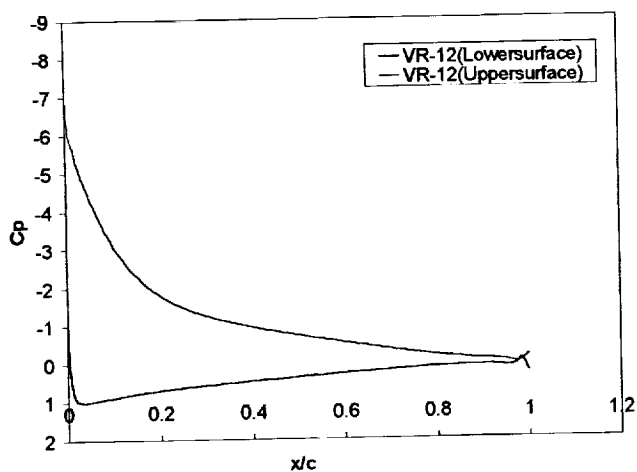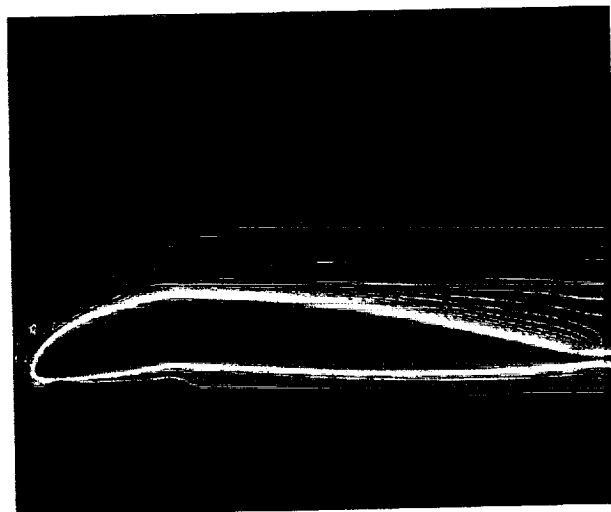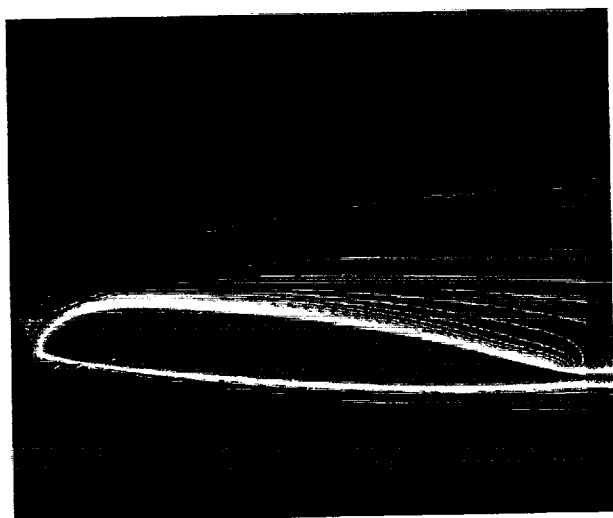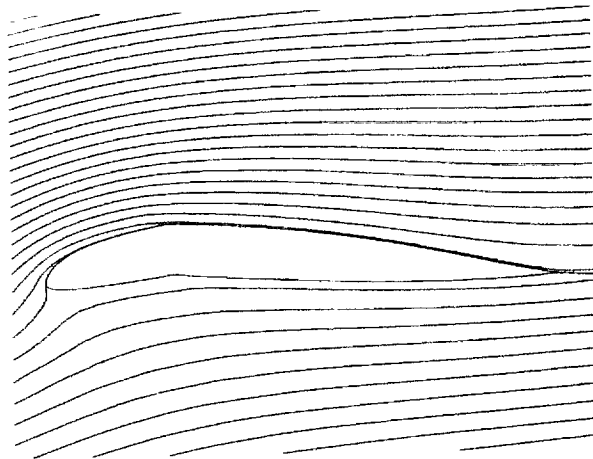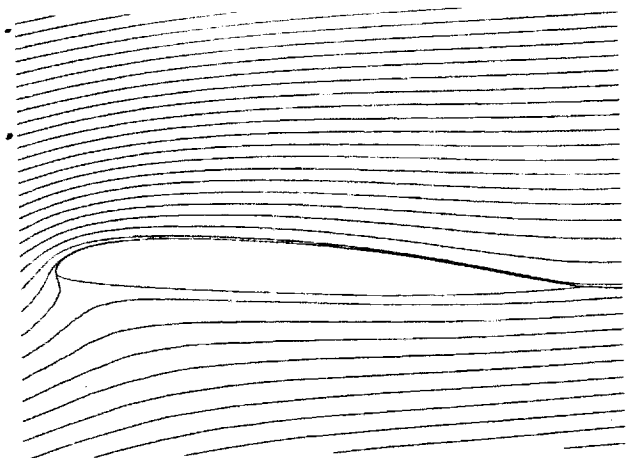
Figures 1.a: Streamlines, Vorticity contours and Surface coefficient over the VR-12 airfoil at α=14 °(down stroke)

Figures 1.b: Streamlines, Vorticity contours and Surface coefficient over the VR-2513 airfoil at α=14 °(down stroke)
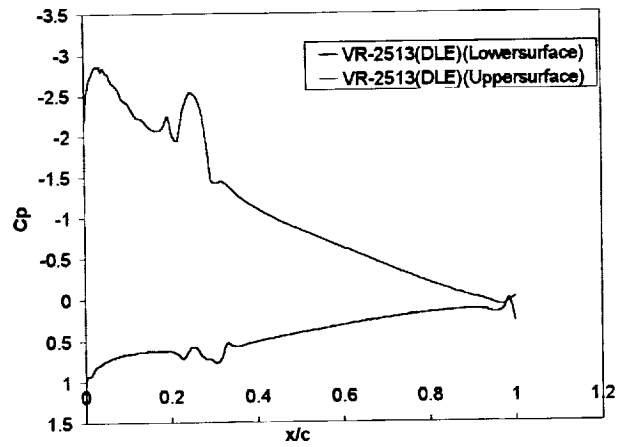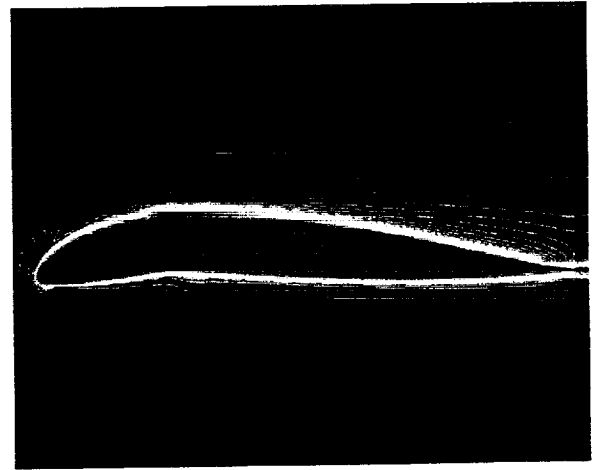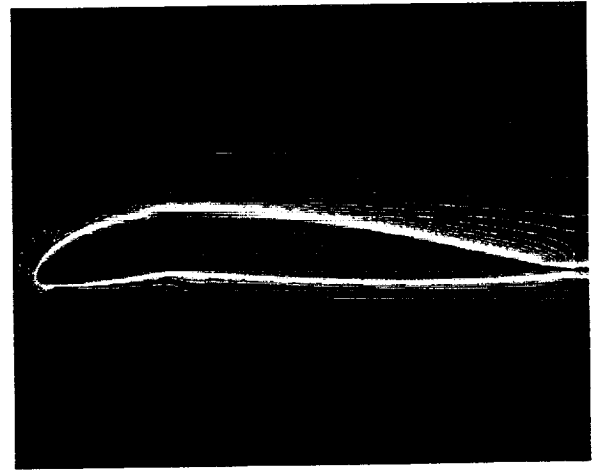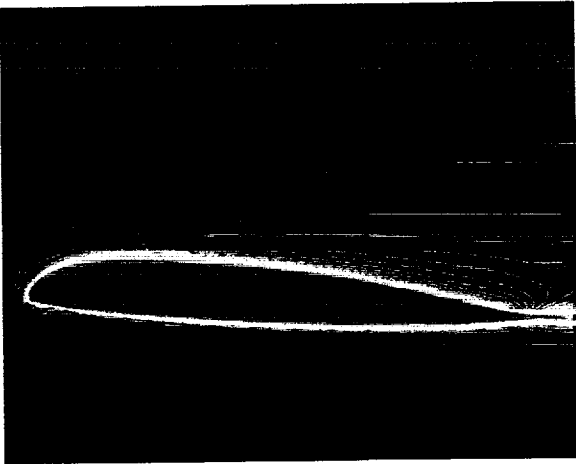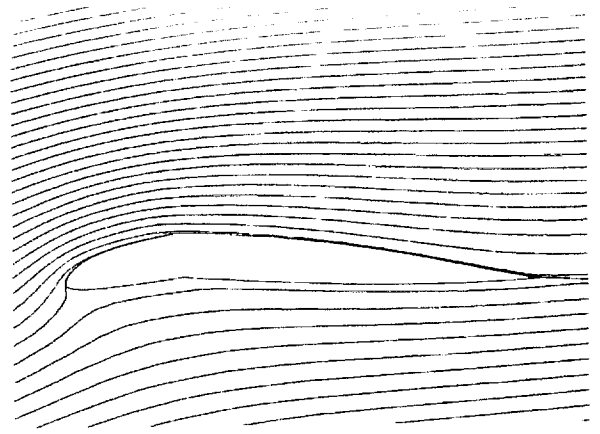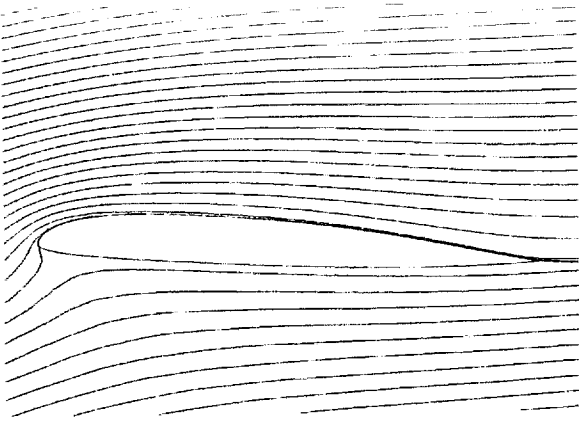
Figures 2.a Streamlines, Vorticity contours and Surface pressure coefficient over the VR-12 airfoil at α=14°(up stroke)


Figures 2.b Streamlines, Vorticity contours and Surface pressure coefficient over the VR-2513 airfoil at α=14°(up stroke)
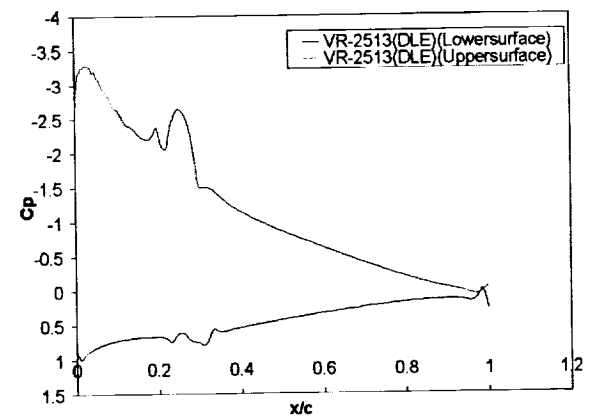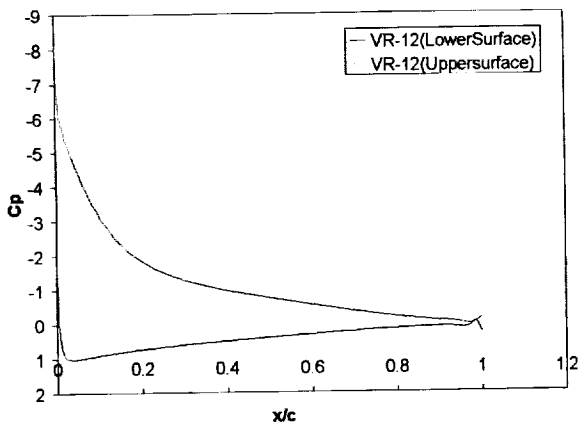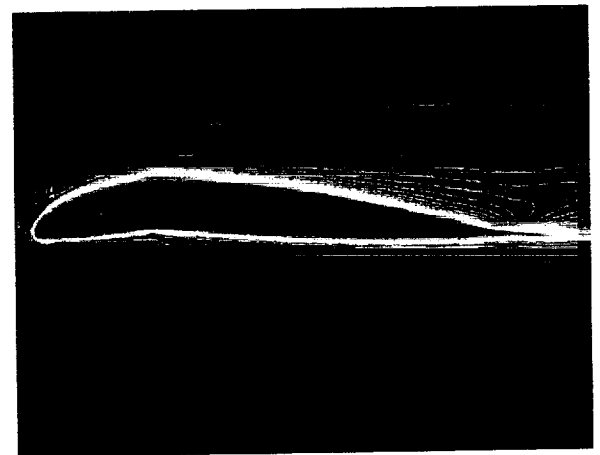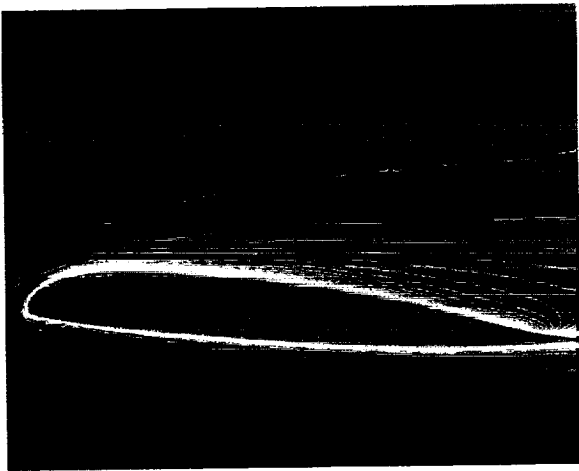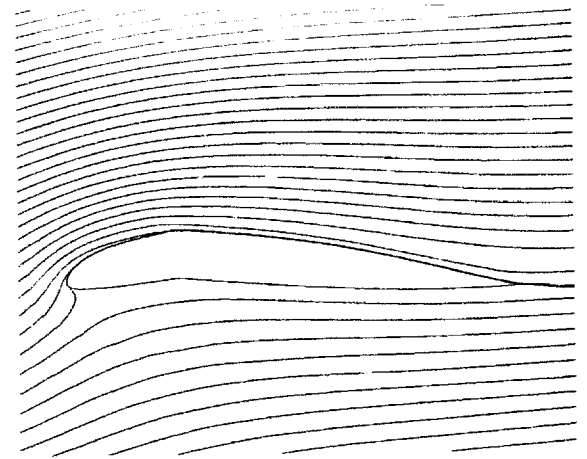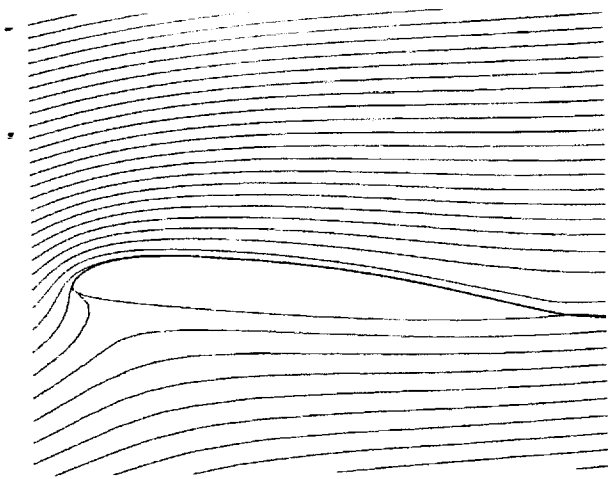
Figures 3.a Streamlines, Vorticity contours and Surface pressure coefficient over the VR-12 airfoil at α=15°(peak)

Figures 3.a Streamlines, Vorticity contours and Surface pressure coefficient over the VR-2513 airfoil at α=15°(peak)
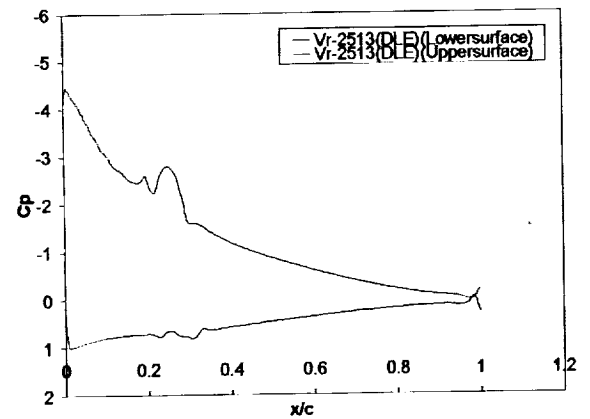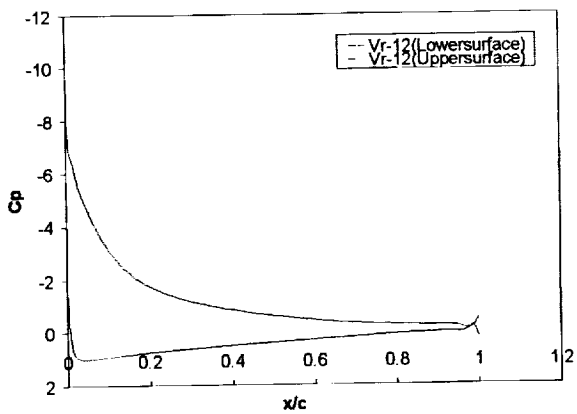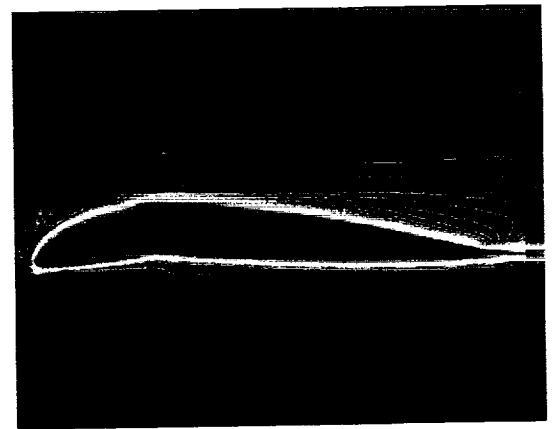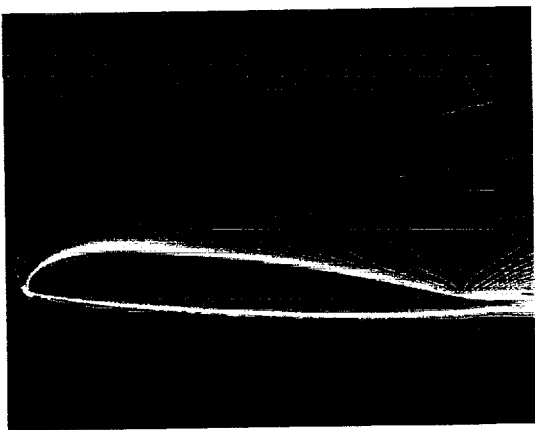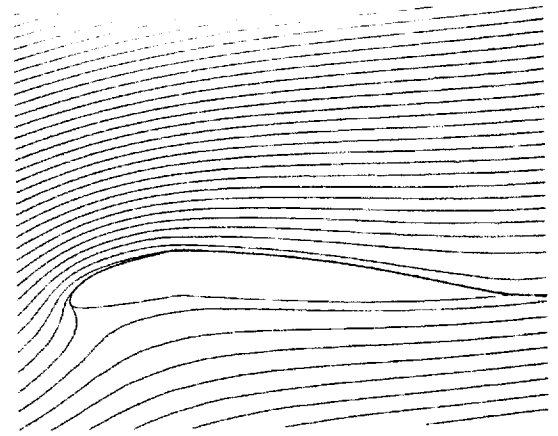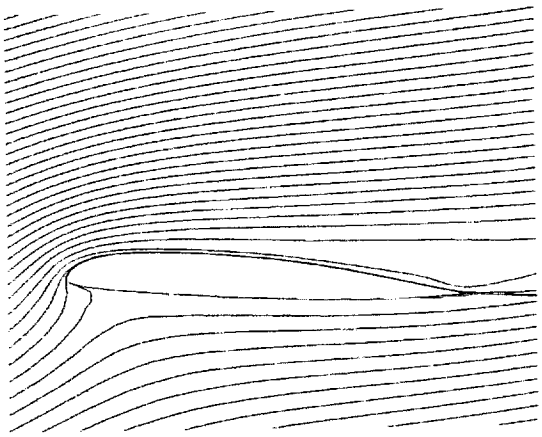
Figures 4.a Streamlines, Vorticity contours and Surface pressure coefficient over the VR-12 airfoil at α=17°(down stroke)

Figures 4.b Streamlines, Vorticity contours and Surface pressure coefficient over the VR-2513 airfoil at α=17°(down stroke)

-12
-10
-8
-6
-4
-2
0
2

Cp

— Vr-12(Lowersurface)
— Vr-12(Uppersurface)

0.2   0.4   0.6   0.8   1   1.2

x/c

-5
-4
-3
-2
-1
0
1
2

Cp

— Vr-2513(DLE)(Lowersurface)
Vr-2513(DLE)(Uppersurface)

0.2   0.4   0.6   0.8   1   1.2

x/c
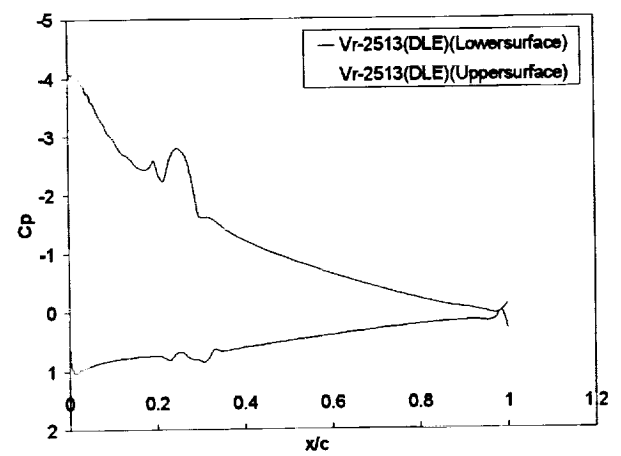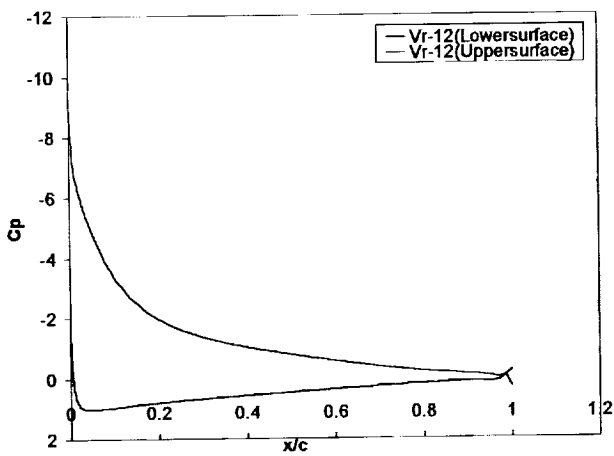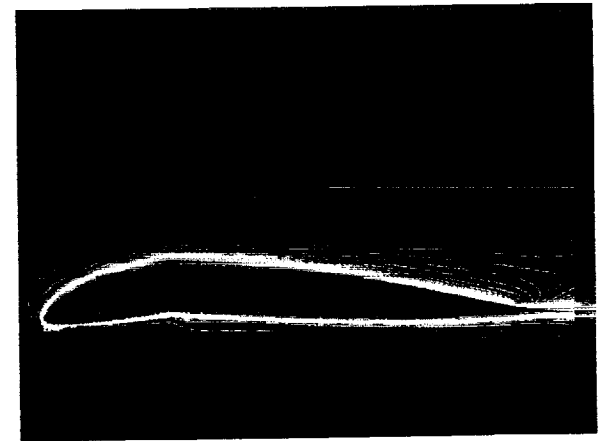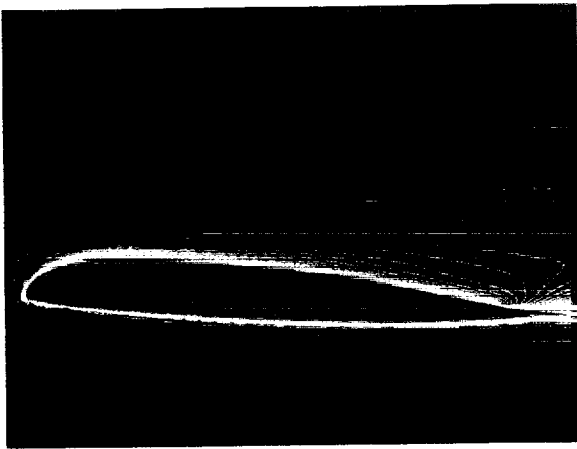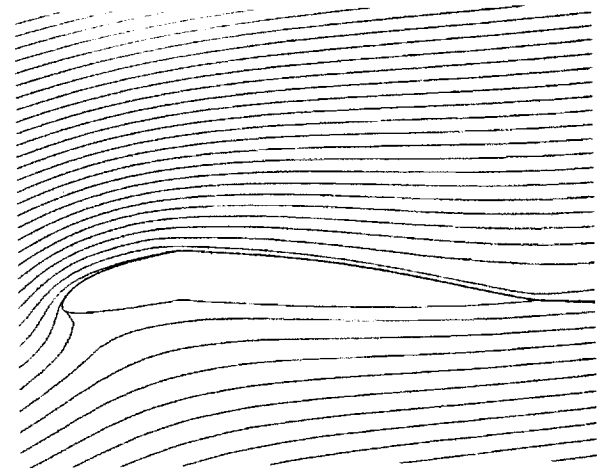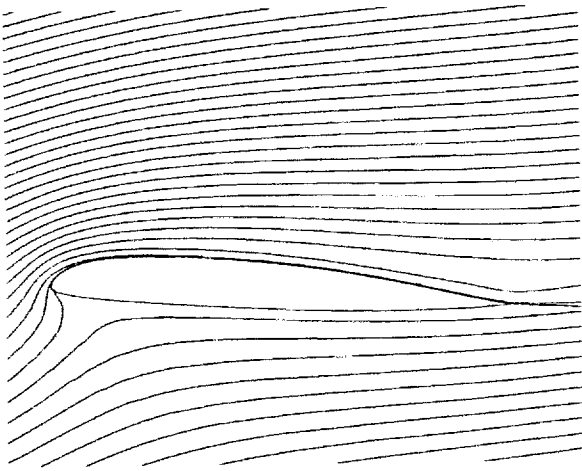
Figures 5.a Streamlines, Vorticity contours and Surface pressure coefficient over the VR-12 airfoil at $\alpha=17°$(up stroke)

Figures 5.b Streamlines, Vorticity contours and Surface pressure coefficient over the VR-2513 airfoil at $\alpha=17°$(up stroke)
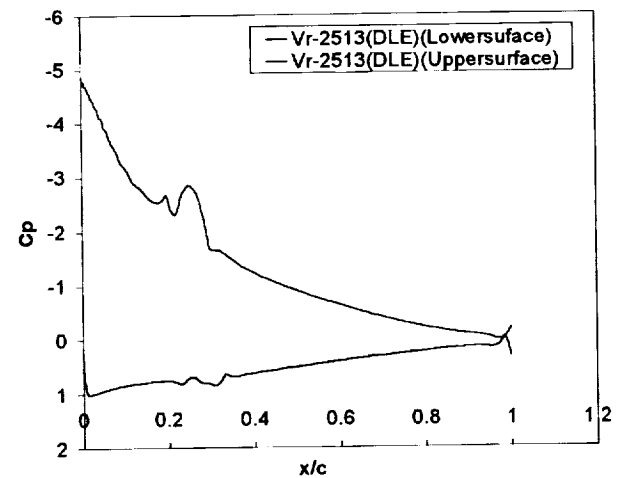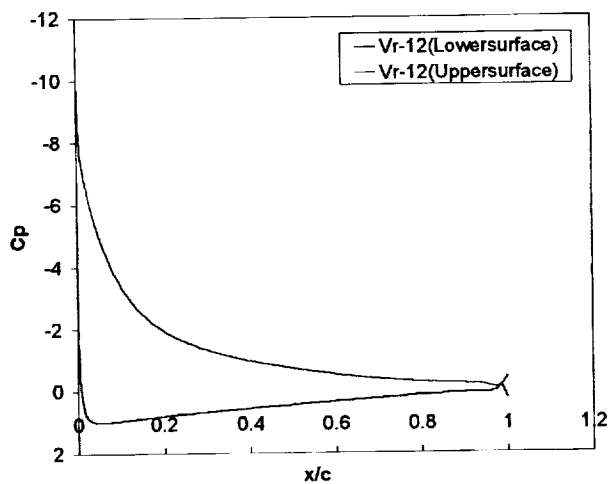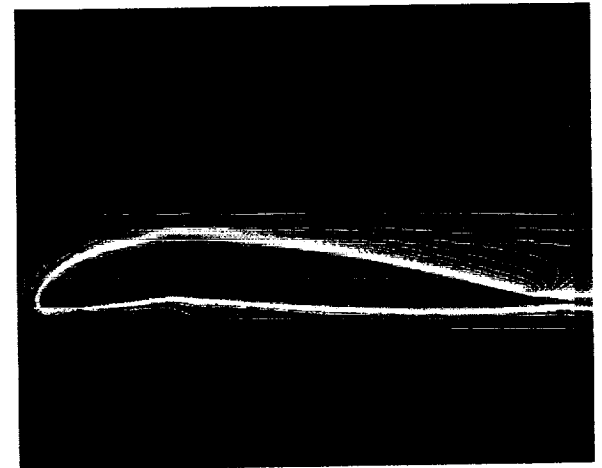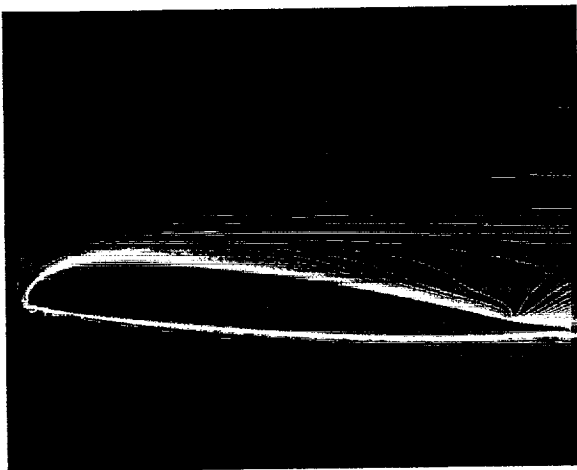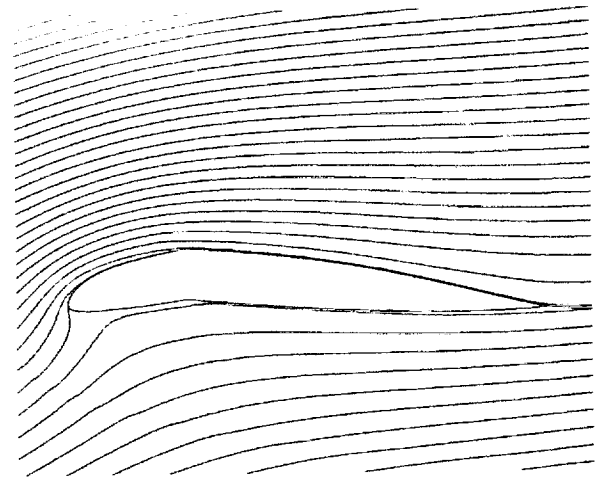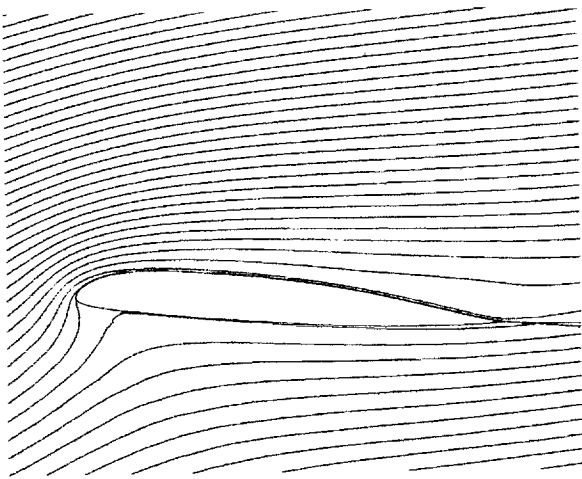
Figures 6.a Streamlines, Vorticity contours and Surface pressure coefficient over the VR-12 airfoil at $\alpha=18°$(peak)

Figures 6.b Streamlines, Vorticity contours and Surface pressure coefficient over the VR-2513 airfoil at $\alpha=18°$(peak)
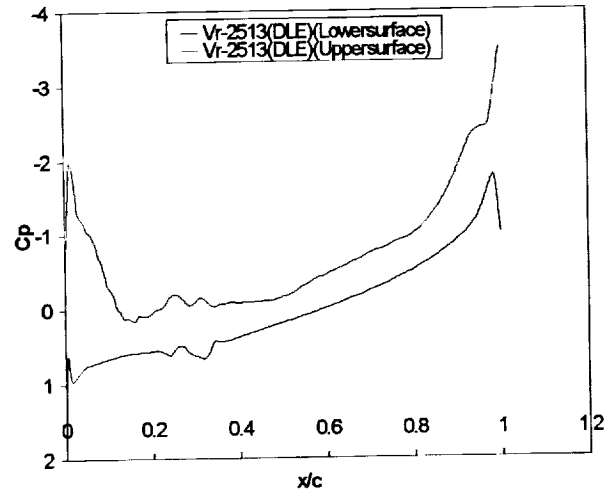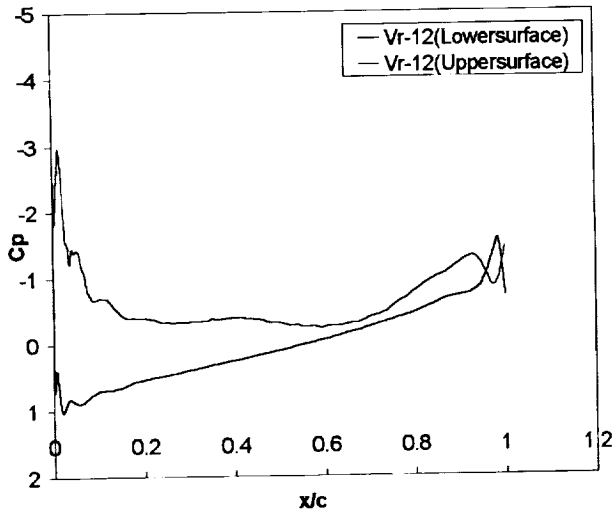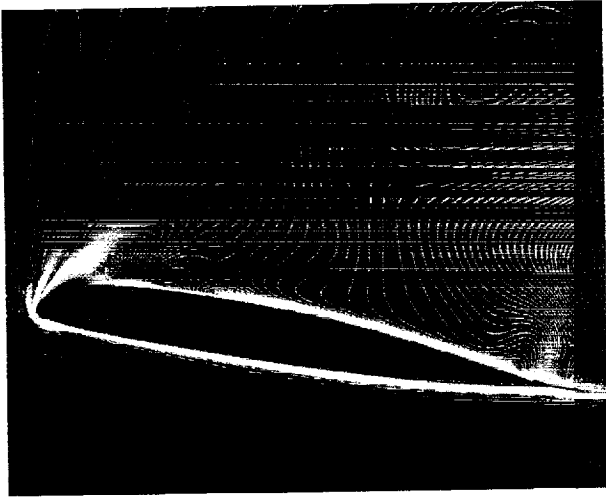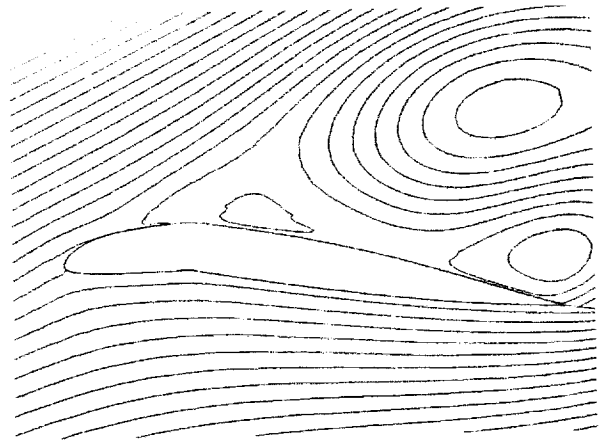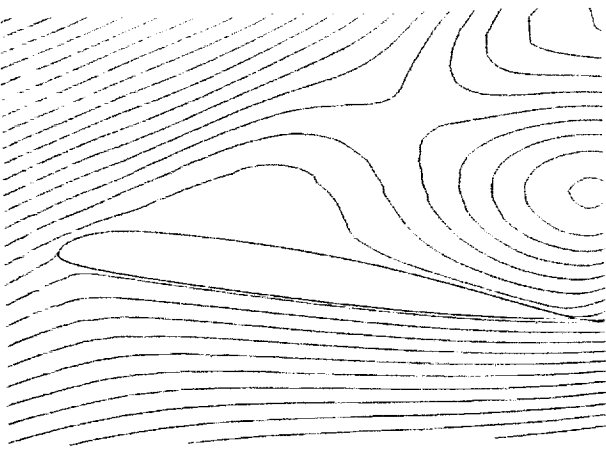
Figures 7.a Streamlines, Vorticity contours and Surface pressure coefficient over the VR-12 airfoil at α=24°(down stroke)

Figures 7.b Streamlines, Vorticity contours and Surface pressure coefficient over the VR-2513 airfoil at α=24°(down stroke)
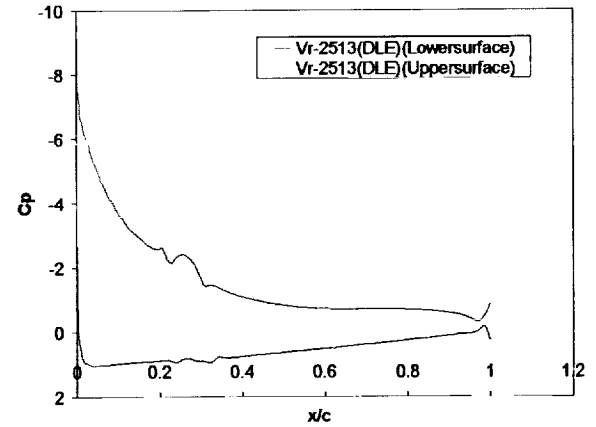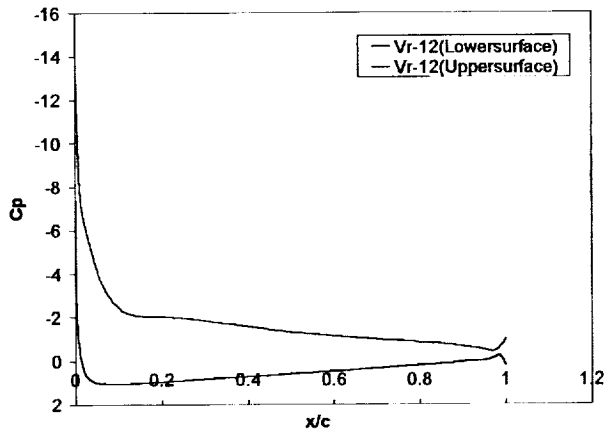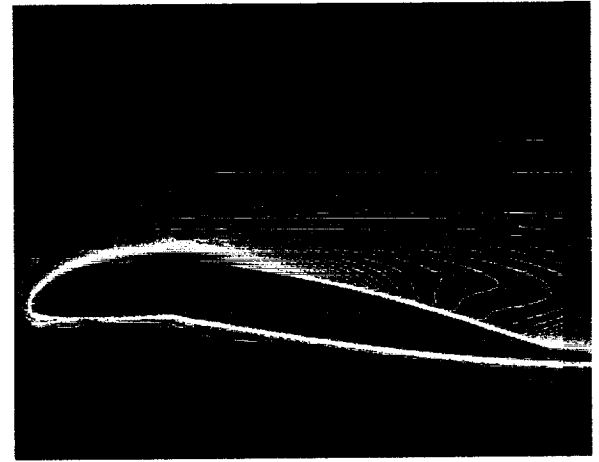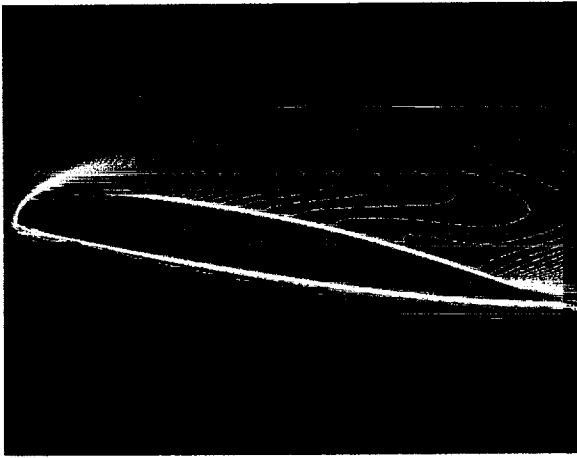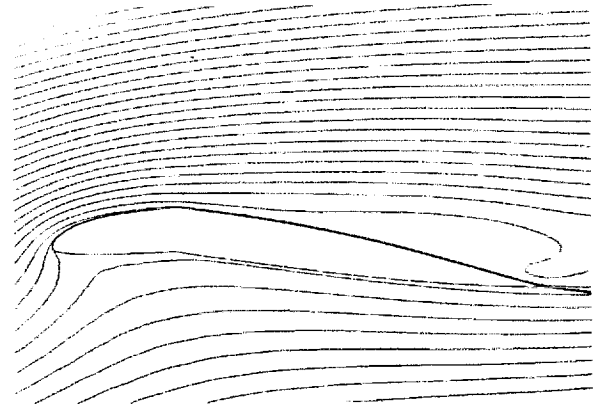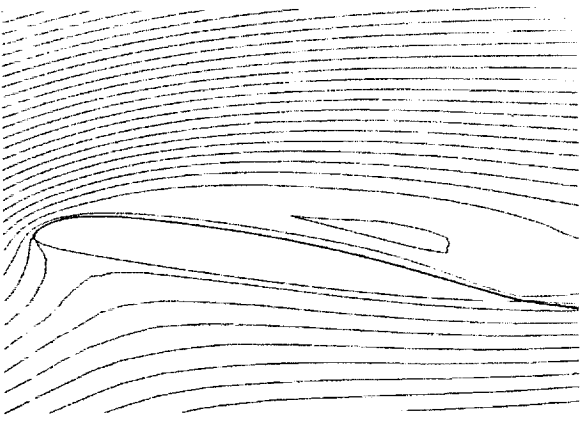
Figures 8.a Streamlines, Vorticity contours and Surface pressure coefficient over the VR-12 airfoil at α=24°(up stroke)

Figures 8.b Streamlines, Vorticity contours and Surface pressure coefficient over the VR-2513 airfoil at α=24°(up stroke)
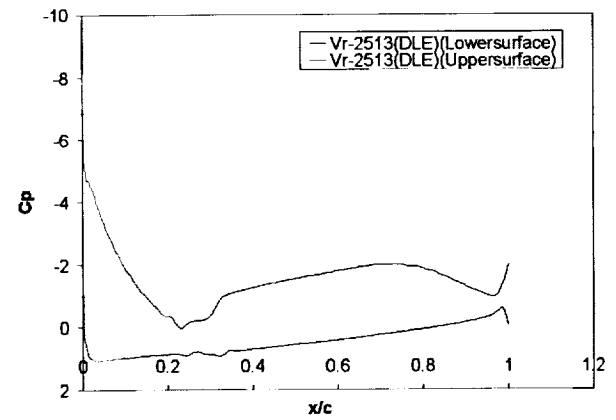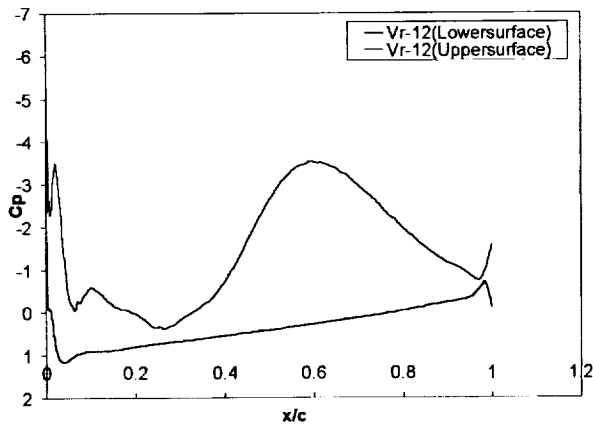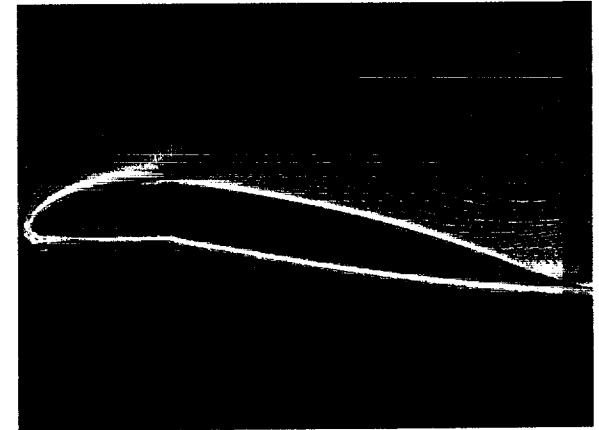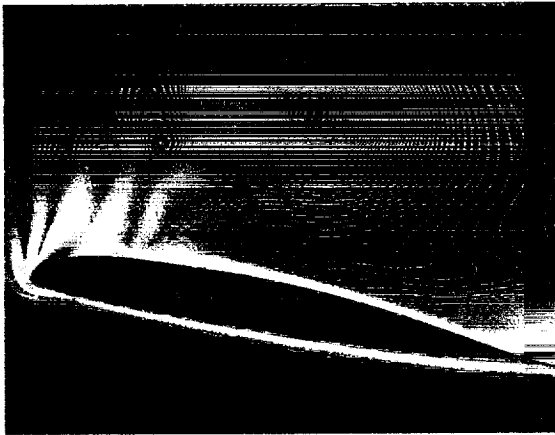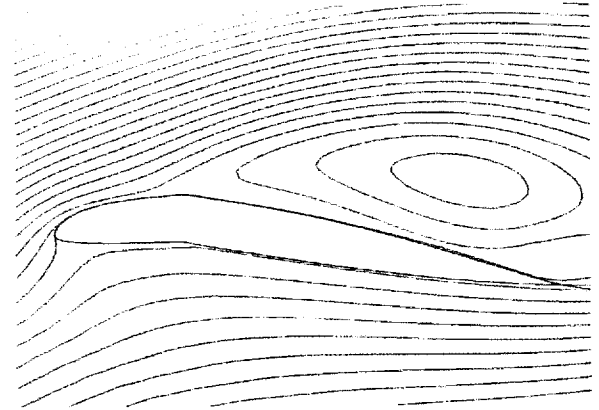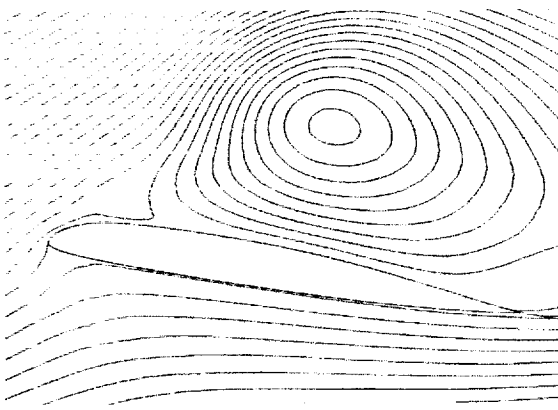
Figures 9.a Streamlines, Vorticity contours and Surface pressure coefficient over the VR-12 airfoil at α=25°(peak)

Figures 9.b Streamlines, Vorticity contours and Surface pressure coefficient over the VR-2513 airfoil at α=25°(peak)
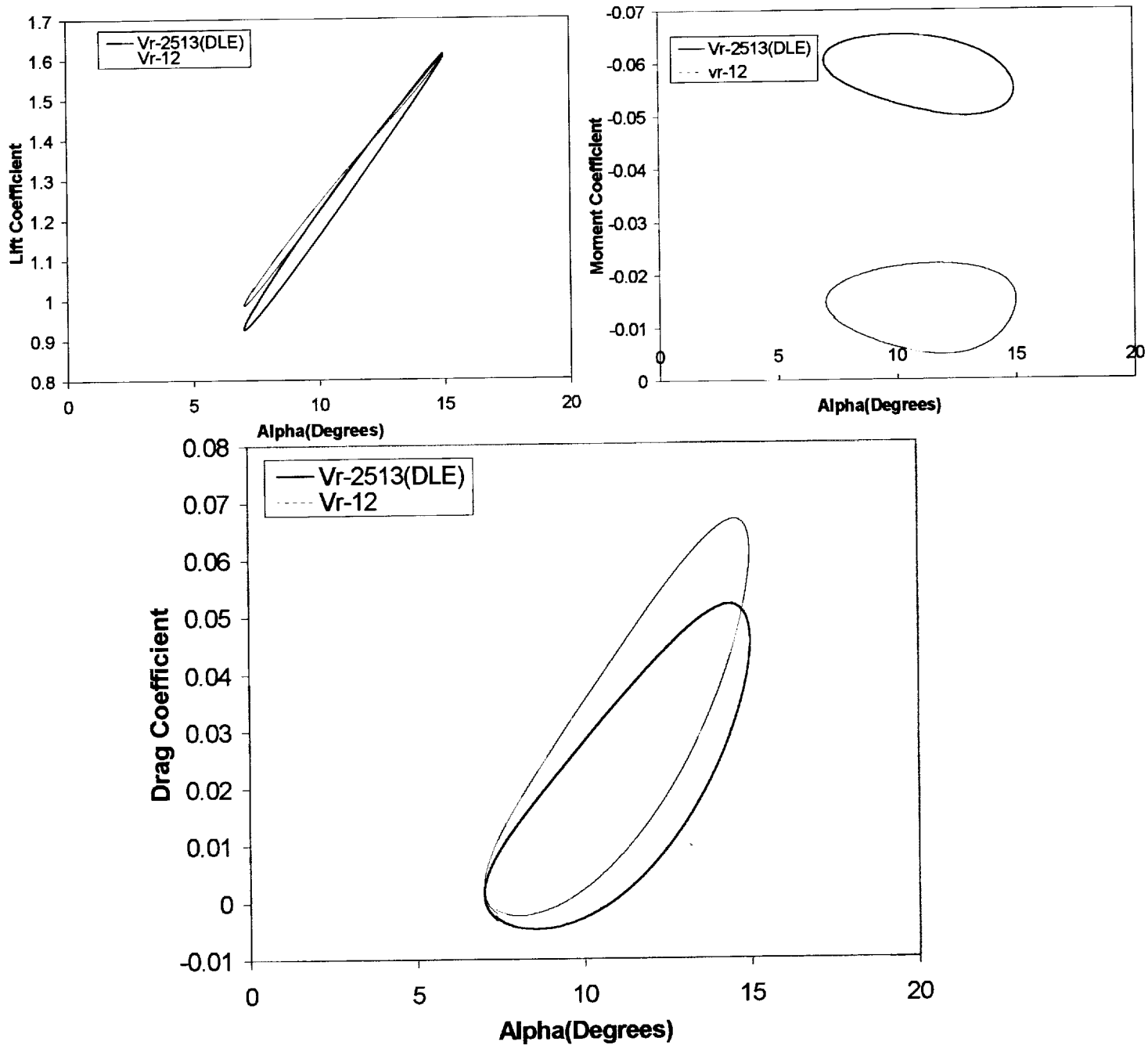
Figure10. Lift, Drag and Pitching Moment Hysteresis Loops for VR-12 and VR-2513 airfoils at $\alpha = 11° \pm 4°\cos(Wt)$.
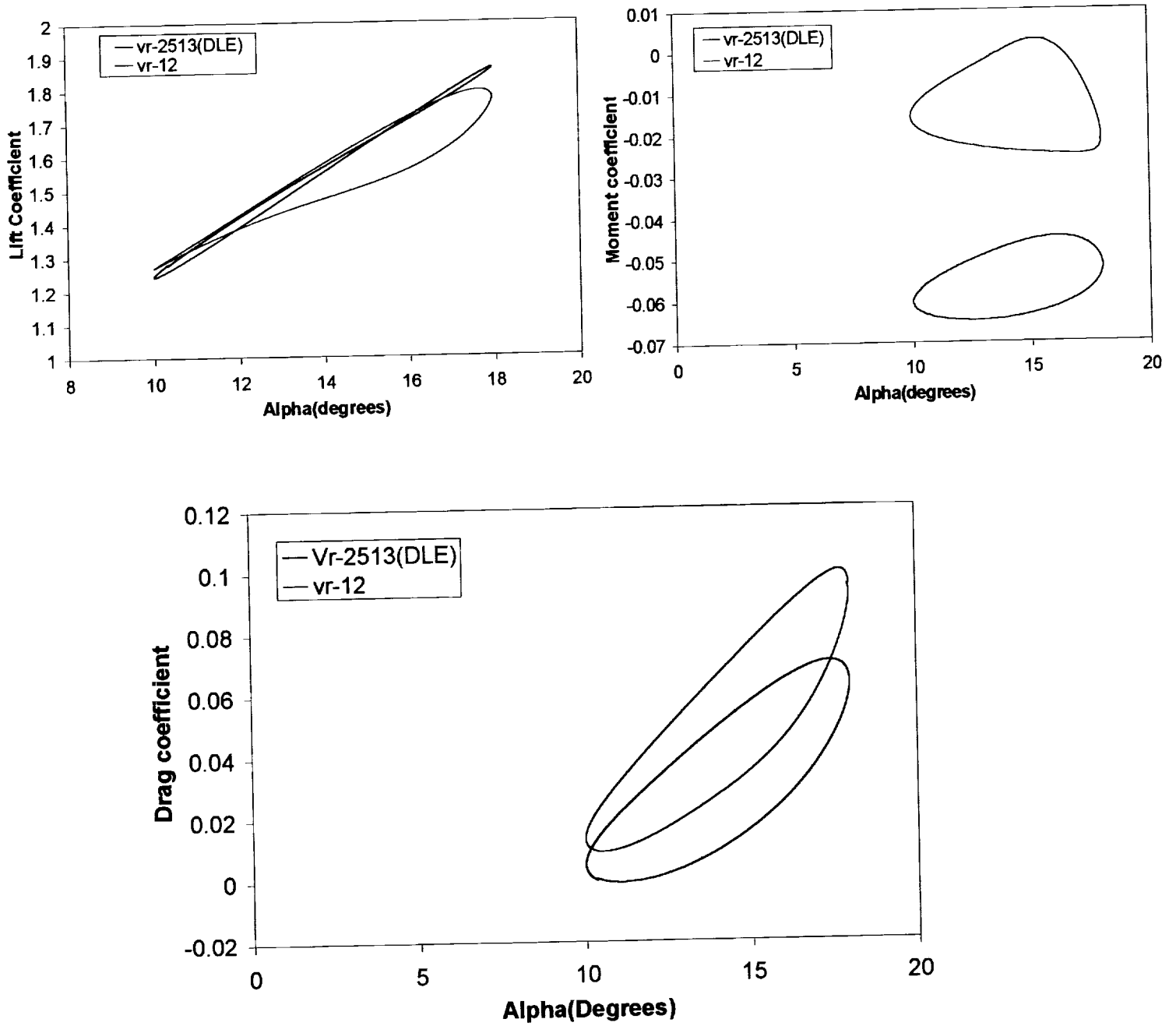
Figure11. Lift, Drag and Pitching Moment Hysteresis Loops for VR-12 and VR-2513 airfoils at $\alpha = 14° \pm 4°\cos(Wt)$.
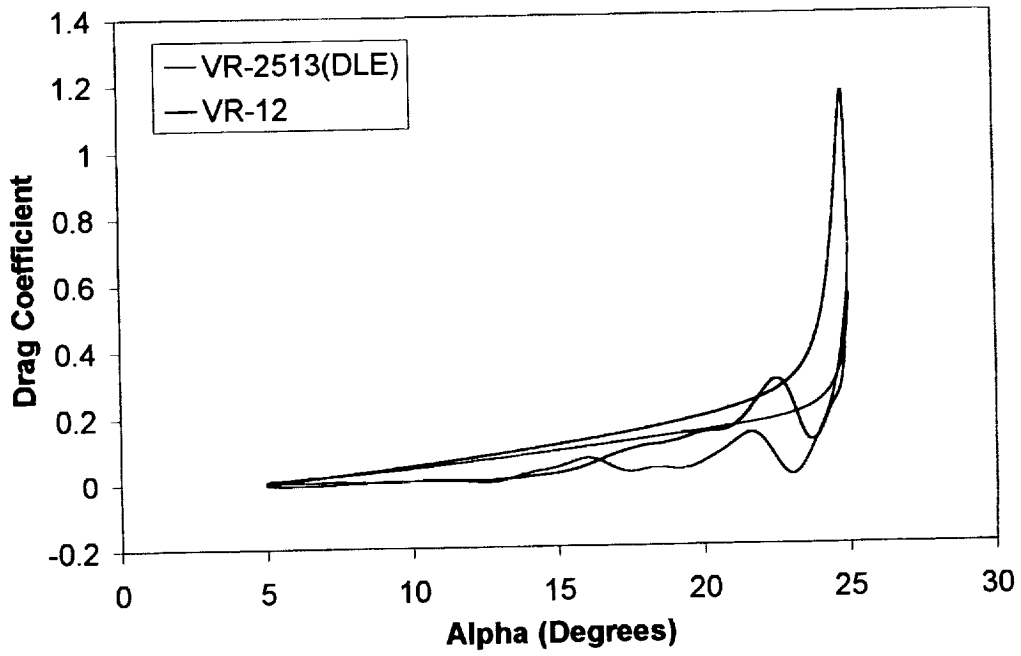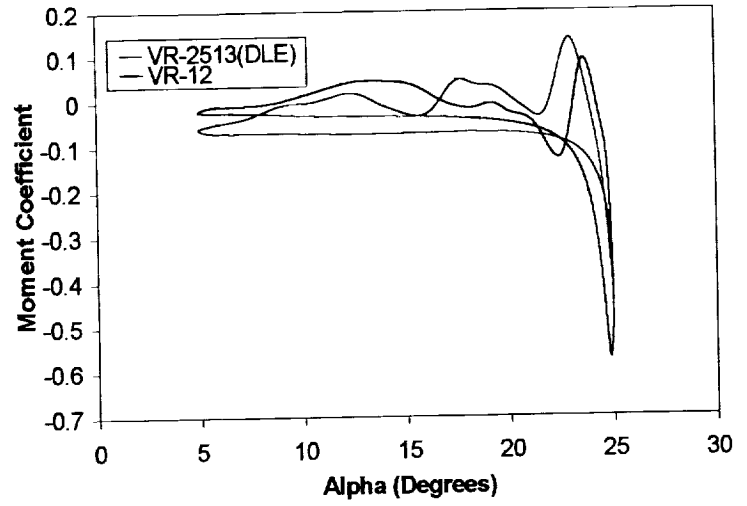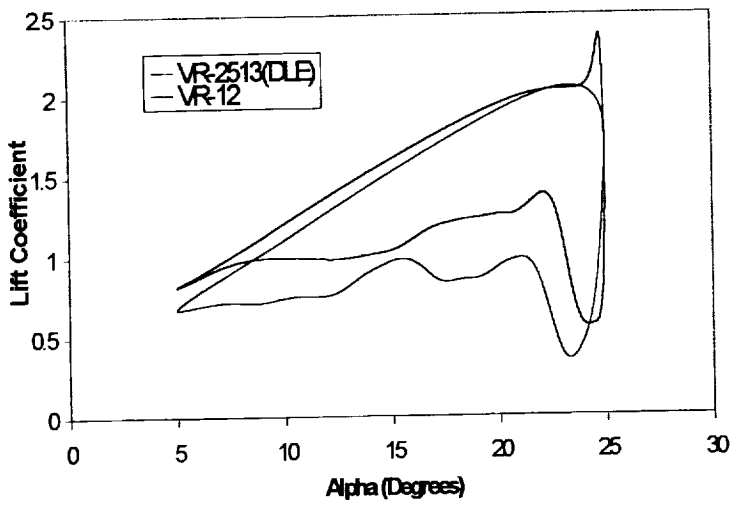
Figure 12. Lift, Drag and Moment Hysteresis Loops for VR-12 and
VR-2513 airfoils at $\alpha = 15° \pm 10°\cos(Wt)$.